

# Water Resources Research

## RESEARCH ARTICLE

10.1029/2021WR030110

### Key Points:

- Time-lapse crosshole ground penetrating radar (GPR) full-waveform inversion (FWI) shows a potential to monitor high-resolution of  $\sim 0.2$  m transport of tracer in aquifer
- Starting model strategies for FWI were tested in order to optimize plume reconstruction, to be used later for field data sets
- Good recovery of conductivity and especially of permittivity changes suggests to monitor adequate tracers by GPR FWI for transport imaging

### Supporting Information:

Supporting Information may be found in the online version of this article.

### Correspondence to:

P. Haruzi,  
[p.haruzi@fz-juelich.de](mailto:p.haruzi@fz-juelich.de)

### Citation:







Haruzi, P., Schmäck, J., Zhou, Z., van der Kruk, J., Vereecken, H., Vanderborght, J., & Klotzsche, A. (2022). Detection of tracer plumes using full-waveform inversion of time-lapse ground penetrating radar data: A numerical study in a high-resolution aquifer model. *Water Resources Research*, 58, e2021WR030110. <https://doi.org/10.1029/2021WR030110>

Received 2 APR 2021  
Accepted 21 APR 2022

© 2022 Forschungszentrum Juelich GmbH.

This is an open access article under the terms of the [Creative Commons Attribution-NonCommercial-NoDerivs License](#), which permits use and distribution in any medium, provided the original work is properly cited, the use is non-commercial and no modifications or adaptations are made.

## Detection of Tracer Plumes Using Full-Waveform Inversion of Time-Lapse Ground Penetrating Radar Data: A Numerical Study in a High-Resolution Aquifer Model

P. Haruzi<sup>1,2,3</sup> , J. Schmäck<sup>1,2</sup> , Z. Zhou<sup>1,2</sup>, J. van der Kruk<sup>1,2</sup> , H. Vereecken<sup>1,2</sup> , J. Vanderborght<sup>1,2</sup> , and A. Klotzsche<sup>1,2</sup> 

<sup>1</sup>Agrosphere Institute, IBG-3, Forschungszentrum Jülich GmbH, Juelich, Germany, <sup>2</sup>Centre for High-Performance Scientific Computing in Terrestrial Systems (HPSC-TerrSys), Geoverbund ABC/J, Juelich, Germany, <sup>3</sup>Department of Environmental Physics and Irrigation, Agricultural Research Organization – Volcani Institute, Rishon LeZion, Israel

**Abstract** Imaging subsurface small-scale features and monitoring transport of tracer plumes at a fine resolution is of interest to characterize transport processes in aquifers. Full-waveform inversion (FWI) of crosshole ground penetrating radar (GPR) measurements enables aquifer characterization at decimeter-scale resolution. The method produces images of both relative dielectric permittivity ( $\epsilon_r$ ) and bulk electrical conductivity ( $\sigma_b$ ) that can be related to hydraulic aquifer properties and tracer distributions. To test the potential of time-lapse GPR FWI for imaging tracer plumes, we conducted a numerical tracer experiment by injecting saline water, desalinated water, and ethanol in a heterogeneous aquifer. The saline and desalinated tracers only changed  $\sigma_b$ , whereas ethanol changed both  $\epsilon_r$  and  $\sigma_b$ . Tracer concentrations were retrieved from the inverted  $\epsilon_r$  and  $\sigma_b$  models using information about petrophysical parameters. GPR FWI  $\epsilon_r$  and  $\sigma_b$  tracer images could recover preferential paths of  $\sim 0.2$  m width, while the derived  $\sigma_b$  structures are smoother. FWI of 50 time-lapse data sets demonstrated the potential of the FWI to derive spatially resolved breakthrough curves of the saline and ethanol tracer in the image plane between the boreholes. Thus, high-resolution imaging with GPR FWI of tracers that produce a high permittivity contrast against the background has a great potential for characterization of heterogeneous transport in aquifers.

## 1. Introduction

Ever increasing water demands and anthropogenic pollution lead to depletion of clean groundwater resources. Detailed knowledge of the flow and transport processes, which control migration of fluids, particles, and solutes in the subsurface (hereafter tracers), is necessary, for example, to protect groundwater pumping wells from pollution and operate remediation measures (Maliva, 2016). Important transport characteristics that need to be known are the tracer velocity, the tracer plume spreading, and the tracer dilution by mixing with groundwater. These transport characteristics depend strongly on the heterogeneity of hydraulic aquifer properties (Cheng & Bear, 2016), which are difficult to observe directly because of the intrinsic inaccessibility of the subsurface. Tracer experiments that monitor tracer plumes in aquifers can be used to determine transport characteristics and infer the underlying hydraulic aquifer properties and their spatial variability (e.g., Vereecken et al., 2000).

Traditional techniques for hydrologic characterization, such as pumping tests, provide data on large-scale aquifer hydraulic properties, but with low spatial resolution (e.g., Li et al., 2007). Other well-established techniques provide fine-scale information in the vertical direction, such as borehole measurements (Englert, 2003), cone penetration tests (Tillman et al., 2008), and measurements on sediment cores (Vereecken et al., 2000), but cannot characterize spatial variability in the horizontal (flow) direction with high spatial resolution. Geophysical imaging techniques such as electrical resistivity tomography (ERT) and ground penetrating radar (GPR) can close this gap in observation capabilities and provide information on an appropriate scale (up to  $\sim 5$ –100 m) and with high spatial resolution in both vertical and horizontal direction, while being minimally invasive (e.g., Binley et al., 2015; Looms et al., 2008). Geophysical imaging methods enable to image the subsurface by sensing changes in the physical parameters of a porous medium. Specifically, relative dielectric permittivity ( $\epsilon_r$ ) and electrical conductivity ( $\sigma$ ) of porous media or an aquifer vary in space and time (Everett, 2013).  $\epsilon_r$  is mainly dominated by the water content and its temperature, while  $\sigma$  depends on the salinity and temperature of the pore water and on the clay content (Everett, 2013). Migration of a tracer through the aquifer changes these aquifer properties so that imaging these changes in a time-lapse manner using dedicated geophysical methods, such as

GPR (Klotzsche, Lärm, et al., 2019; Looms et al., 2008), and ERT (Hermans et al., 2015; Kemna et al., 2002; Singha & Gorelick, 2005), can be used to image the tracer plume. Whereas ERT measurements are made using direct current and provide bulk electrical conductivity ( $\sigma_b$ ), GPR operates in a high-frequency range (typically 10–2,600 MHz) and uses the propagation of the electromagnetic (EM) wave in resistive earth materials. In contrast to ERT, GPR can provide both  $\epsilon_r$  and  $\sigma_b$ . While the velocity of the EM wave can be linked to  $\epsilon_r$ , the attenuation of the EM wave provides information about the  $\sigma_b$  (Annan, 2009). High-frequency GPR systems allow higher imaging resolution of the subsurface that scales with the wavelength ( $\lambda$ ) of the measured signal. For a typical used frequency ( $f$ ) spectra of 10–200 MHz (the range used in this study) of the EM signal and a  $\epsilon_r$  of 12–25 of the media, the wavelength scales between 0.3 and 8.5 m ( $\lambda(\epsilon_r, f) = c_0/\sqrt{\epsilon_r f}$ ; with  $c_0 = 3 \times 10^8$  m/s as the EM velocity in air (Annan, 2009)). Especially, GPR acquisition in a wave transmission configuration with transmitters in one borehole and receivers in another (crosshole) (Huisman et al., 2003; Klotzsche, Vereecken, & van der Kruk, 2019) allows a good subsurface illumination with dense ray-coverage and relatively small acquisition errors (Axtell et al., 2016). Time-lapse crosshole GPR monitoring of fluid transport using ray-based tomography was successful in illuminating preferential pathways from either signal attenuation due to a saline tracer of about 2 m width in a fractured rock (Day-Lewis et al., 2003), or wave velocity changes due to soil water content changes at a decimeter scale (Looms et al., 2008).

Crosshole GPR data is measured mainly in multi-offset gather (MOG) measurements and commonly imaged with ray-based tomography. Velocity distributions, from which  $\epsilon_r$  images are derived, are obtained from the first arrival travel times of the wave signals (e.g., Dafflon et al., 2011), and attenuation tomograms of the subsurface, from which  $\sigma_b$  images can be estimated, are obtained from first-cycle amplitudes (Holliger et al., 2001). The ray-based approach, which uses only specific features of the recorded traces, can provide tomograms with a resolution that scales with the wavelength of the center frequency of the used signals. In contrast, GPR full-waveform inversion (FWI) uses the full information content of the received signal, what ultimately improves the resolution of the  $\epsilon_r$  and  $\sigma_b$  tomograms below the wavelength scale (Klotzsche, Vereecken, & van der Kruk, 2019). Time-domain crosshole GPR FWI was applied in the last decade to more than 40 different data sets from various test sites and demonstrated the possibility to characterize aquifers within decimeter-scale resolution including important small-scale structures like high porosity zones and impermeable clay lenses (overview provided by Klotzsche, Vereecken, and van der Kruk [2019]). Gueting et al. (2015, 2017, 2020) demonstrated that 2D crosshole GPR FWI results could identify aquifer layers of a few decimeters thickness. This high-resolution reconstruction of layers allowed to explain previously observed tracer plume transport and in particular tracer plume splitting (Müller et al., 2010) that was caused by the presence of a thin layer with a lower hydraulic conductivity. In general, crosshole GPR is more sensitive in the inter-well region and over a larger area than crosshole ERT, which is more sensitive near the boreholes (Day-Lewis et al., 2005). Additionally, GPR can provide higher-resolution images than ERT.

Next to spatial resolution, another problem in geophysical imaging is the translation of imaged parameters ( $\epsilon_r$  and  $\sigma_b$  in GPR) to the property of interest, the tracer or substance concentration. Since the petrophysical relations between them depend on spatially variable aquifer properties like porosity (CRIM model, Birchak et al., 1974), pore structure (Archie, 1942), and surface charge density of the mineral surfaces (Rhoades, 1981), such relationships are site dependent and spatially variable (e.g., Müller et al., 2010). The translation of the imaged electric properties to concentration distribution is therefore afflicted by this spatial variability. Utilizing high-resolution GPR FWI before tracer injection can be used to reduce the uncertainty in such petrophysical relations. Some petrophysical parameters such as the porosity that is, used in the CRIM model and the formation factor used in Archie's Law can be calculated directly for each pixel of the background models that are obtained by FWI of GPR data sets that are acquired before tracer injection. Furthermore, it is expected that these results are significantly better and higher in resolution than traditional time-lapse ray-based inversion approaches.

In this study, we analyze the potential of time-lapse crosshole GPR FWI for imaging tracer tests in heterogeneous aquifers, using a numerical experiment. The setup of the experiment is based on the properties of the aquifer at the Krauthausen test site, which consists of heterogeneous alluvial sandy-gravel sediments showing preferential flow paths with thicknesses of  $\sim 0.2$  m (Gueting et al., 2017). Generating a realistic high-resolution aquifer and transport model to generate the plume fate enables a thoughtful consideration for site-specific design and measurement planning. Different tracer scenarios were analyzed using a salt and an ethanol tracer. Through petrophysical relations the plume concentrations (a) of positive/negative salt tracers were converted to increases/decreases

in  $\sigma_b$ , and (b) of an ethanol tracer to decreases in both  $\sigma_b$  and  $\epsilon_r$ . Note, commonly, only changes in  $\sigma_b$  from salt (Kemna et al., 2002) and heat (Hermans et al., 2015) tracers are imaged with methods like ERT. Since the GPR FWI provides both high-resolution  $\epsilon_r$  and  $\sigma_b$  images, we want to evaluate the potential of imaging tracer distributions from both parameters. Crosshole GPR data were generated before and during the plume intrusion. We tested the ability of FWI to recover the tracer distribution for different tracer concentrations that generated different changes and contrasts in  $\epsilon_r$  and  $\sigma_b$ . To monitor tracer experiments, we tested different FWI starting models for  $\epsilon_r$  and  $\sigma_b$  based on a high resolution FWI models of the previous time step or of the background (Asnaashari et al., 2015; Zhang & Huang, 2013). For quantitative evaluation of the plume recovery, we calculated the coefficient of correlation between the “real” and recovered concentration and compared their wavelength spectra. A qualitative assessment of the recovery of the plume structure was obtained by visual inspection. Finally, we performed an intensive study using 50 time-lapse GPR FWI to predict temporal breakthrough curves for each of the cells of the recovered tomograms.

## 2. Realistic Hydrological Aquifer Model

To realistically model time-lapse GPR data and perform the FWI for the different tracer scenarios, we developed a realistic hydrological model domain of an aquifer in which we simulated flow and transport processes. This model represents an aquifer with a very high spatial resolution, which is necessary to demonstrate the potential of the FWI to reconstruct small-scale structures and hence plume spreading. To achieve this, we used the detailed database and knowledge from the Krauthausen test site in Germany (see Tillmann et al. [2008] and Gueting et al. [2017] for more details).

### 2.1. Krauthausen Test Site as Aquifer Model Domain

We modeled the Krauthausen aquifer that was investigated in many different studies (overview provided in Text S1 of Supporting Information S1). With respect to GPR, the aquifer is well suited due to its low to intermediate electrical conductivity between 5 and 20 mS/m (Zhou et al., 2021). As a first step, we adopted the 3D facies model (Figure 1a) from Gueting et al. (2017, 2018), which was generated based on adjoint tomograms from 2D GPR full-waveform inversions, and subsequently expanded to a 3D cube using multiple-point statistics. This model is composed of three facies: sandy gravel, sand, and gravel. The model covers a domain size of  $20.07 \times 30.15 \times 4.68$  m, from 3.58 to 8.26 m depth and this is composed of cubic cells with an edge size of 0.09 m. Second, we generated the distributions of four aquifer parameters (hydraulic conductivity  $K$ , porosity  $\phi$ , relative permittivity  $\epsilon_r$ , bulk electrical conductivity  $\sigma_b$ ), in each of the three facies using stochastic Gaussian simulation (SGSIM) based on variogram modeling (SGeMS software, Remy et al., 2009). For each property and facies (see Figures 1b–1e), stochastic simulations were performed over the entire model domain. The resulting models were then integrated into one aquifer model domain (“cookie-cutter”) based on the 3D facies distribution.  $K$  and  $\phi$  models were simulated independently with no spatial cross correlation,  $\epsilon_r$  was calculated directly from the  $\phi$  model using the CRIM model (Birchak et al., 1974), and  $\sigma_b$  was simulated using sequential Gaussian co-simulation (COSGSIM) based on the  $\epsilon_r$  spatial distribution as a secondary information with correlation  $r = 0.5$  in each facies (Gueting et al., 2015, 2020). For all the stochastic simulations an exponential variogram model was used (Gringarten & Deutsch, 2001).

### 2.2. Tracer Transport Simulation

We used a flow and transport model based on the designed aquifer model domain to imitate the past positive saline tracer test performed by Müller et al. (2010). The results of Müller et al. (2010) are used in our study as reference for the synthetic plume fate reconstruction. The 3D flow equation was solved using TRACE (Vereecken et al., 1994) and the transport equation was solved using a random-walk particle-tracking algorithm PARTRACE (Bechtold et al., 2011). We simulated a tracer injection for 7 days using a uniform water influx source of 20 m<sup>3</sup>/day between 3.58 and 8.26 m depth in the borehole, and a particle injection source of  $1 \times 10^8$  “conservative or non-reactive” particles which were injected uniformly through the injection period, resulting in an injection concentration of  $7.15 \times 10^5$  particles/m<sup>3</sup>. We modeled the borehole (diam. 50.8 mm, slots 0.5 mm) by a vertical column of grid cells (cubic, edge of 0.09 m) assigned with  $K = 267$  m/d (Klotz, 1990) and a porosity of 1. The borehole was surrounded by a gravel pack that fills the well (diam. 0.328 m), modeled by eight grid cell columns

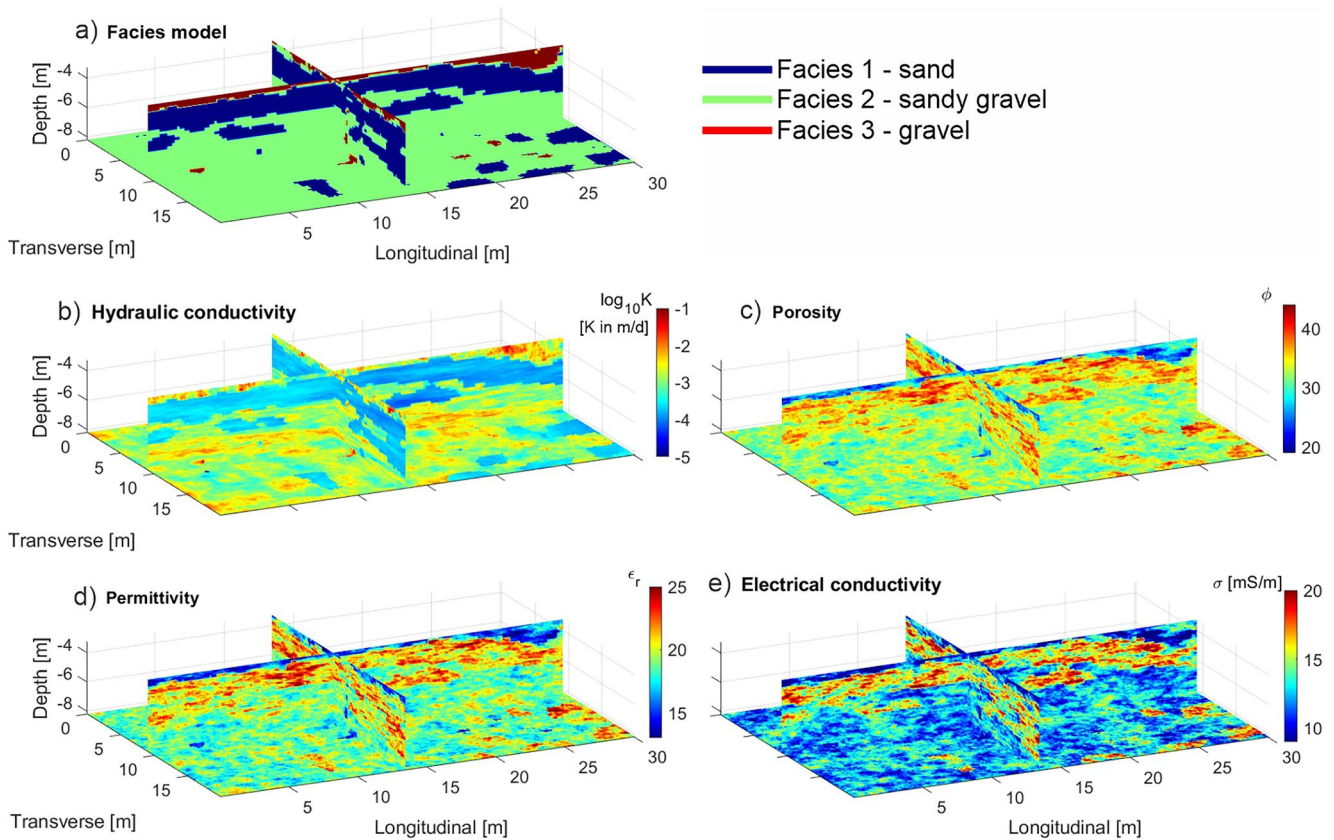


**Figure 1.** Aquifer model domains used for the hydrological flow and transport modeling. (a) Facies model (adopted from Gueting et al. [2018]), (b) log-conductivity, (c) porosity model, (d) background relative permittivity, and (e) electrical conductivity.

with  $K = 2,246$  m/d (Klotz, 1977) and a porosity 0.4. To solve for the total head and velocity distributions in the heterogeneous aquifer, we adopted a natural hydraulic gradient in the aquifer of 0.002 m/m (Vereecken et al., 2000) implemented by pressure head boundary conditions at the up and downstream boundaries, and zero flux conditions at the lateral, top and bottom boundaries. During the injection phase, we used the flow velocity field that was simulated considering the water injection in the well for the transport simulation. After the injection ceased, we simulated the tracer transport using a velocity field that represents the natural hydraulic gradient of the Krauthausen test site. The heterogeneity of the simulated plume was controlled by the stochastically generated  $\ln K$  and porosity (Table S1 in Supporting Information S1), which generated a variable fluid velocity. To account for the effect of velocity fluctuations on solute transport at the grid-cell scale, we used longitudinal and transverse dispersivities of 0.003 and 0.001 m, respectively.

The high-resolution aquifer model can predict transport processes with high spatial resolution as shown for day 15 after the start of the injection (Figure 2). In each plane view, the distribution of mass represents the sum of particle mass along the perpendicular axis to that plane. A substantial part of the plume was transported over a large distance in the lower part of the aquifer (between 7 and 8 m depth), whereas a second part of the plume was moving slower between roughly 5 and 6.5 m depth. The plume is mainly transported in facies 2, which has a higher hydraulic conductivity than facies 1, whereas facies 3 (with the highest conductivity) was barely present within the range of depths where the tracer was injected.

This high-resolution flow and transport model allows us to compare the simulated tracer distribution at monitoring planes with the ERT results from the Krauthausen test site (Figure 3). Note that injection well and injection rate in the simulation were the same as the ones of the real tracer experiment for which the ERT images were obtained. For example, 15 days after the injection started, we can observe a splitting of the simulated plume in a transverse view, similar to the ERT images (Figures 3b and 3c). The general similarity between simulated and ERT observed patterns suggests that the reconstructed facies distribution satisfactorily represents the true



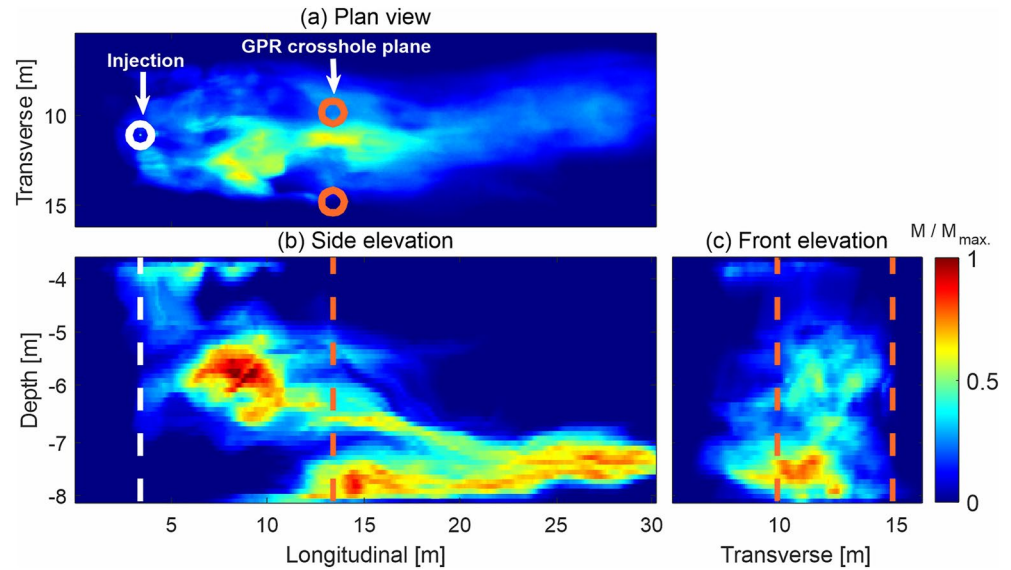


**Figure 2.** Normalized particles mass in (a) plan, (b) side, and (c) front view at day 15 after beginning of the tracer injection. The mass shown is a sum of mass in a line of cells perpendicular to the view. Color maps are normalized to the maximum mass for each view. Boreholes, which are used to derive the ground penetrating radar data, are located 10 m down gradient from the injection well and are illustrated by orange circles and dashed lines.

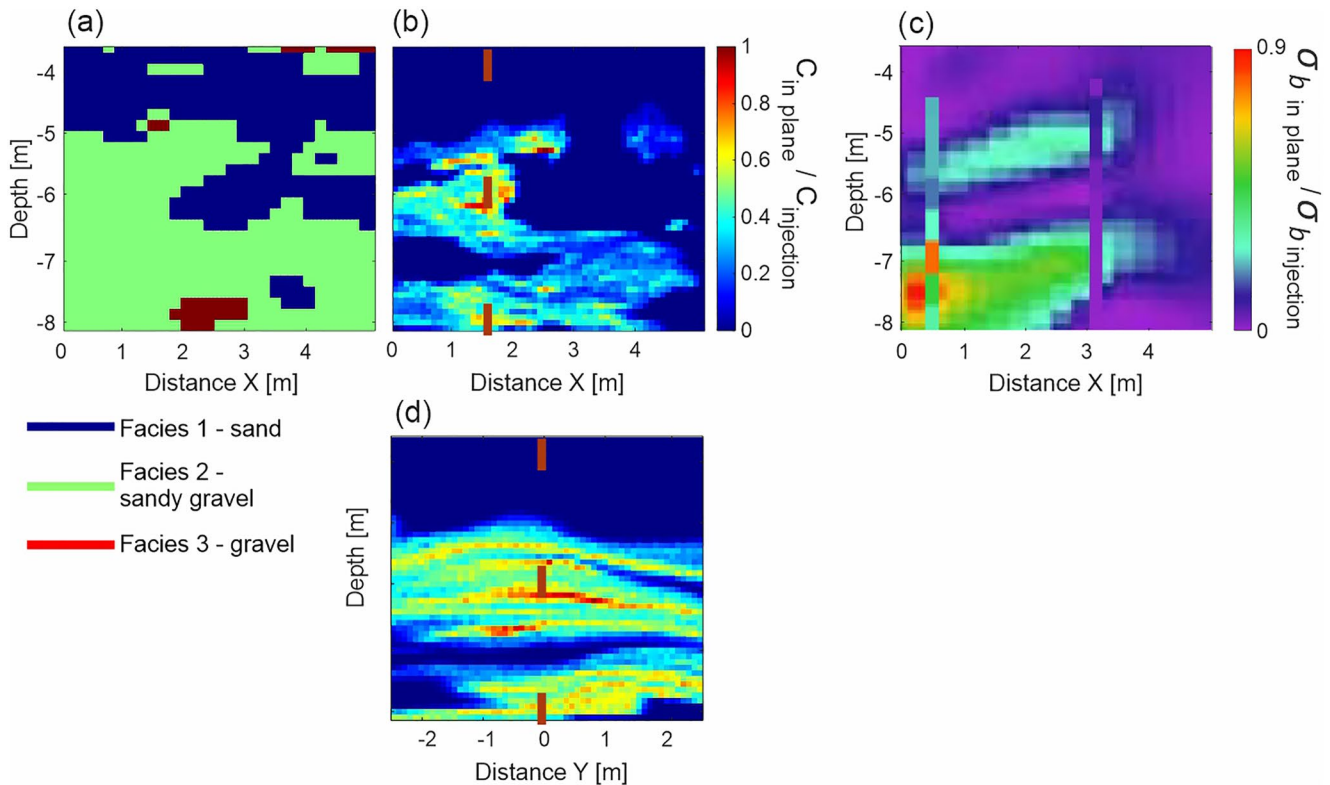


**Figure 3.** Tracer distribution in the monitoring plane. (a) Facies model, (b and d) concentration distribution in transverse and longitudinal directions, and (c) electrical resistivity tomography (ERT) image (modified from Müller et al. [2010], Figure 5) for the domain of the plane between the two ground penetrating radar monitoring boreholes 10 m downgradient from the injection borehole (see Figure 2). The concentration represented the distribution after day 15 from the transport simulation normalized to injected tracer distribution. The red dashed lines in the perpendicular stitching tomograms (b and d) represent the stitching location. The electrical conductivity image is derived from the ERT tomogram and borehole loggers from a previous tracer test at day 15 after beginning the injection. Note that the logger data was obtained in two boreholes (seen as vertical anomalies) with vertical intervals of 0.35 m. The color scale represents the bulk electrical conductivity difference.

distribution. Note that the ERT images did not resolve small-scale tracer concentration variations and the results are more smoothed (Figure 3d). The simulated tracer distribution as imaged in longitudinal view (Figure 3d) is characterized by thin horizontal lenses of 0.1 m thickness with high concentrations (e.g., at 6.2 m depth), which corresponds with the vertical correlation length of  $I_v = 0.18$  m of the hydraulic conductivity in facies 2.

### 3. Tracer Types and Petrophysical Relations

#### 3.1. Change Only in Electrical Conductivity: Salt and Desalinated Water Tracer

The concentration of electrolytes in the groundwater determines the electrical conductivity of the fluid phase, whereas it has only minor influence on the permittivity (Hagrey, 2000; Sreenivas et al., 1995). For pore fluid conductivities that are smaller than  $\sim 15$  S/m, the fluid electrical conductivity is proportional to the equivalent electrical charge concentration (Sreenivas et al., 1995). Salt tracers with a higher concentration are not often imaged with GPR in transmission mode, because of the high attenuation of the EM wave and the restriction of the ray-based approaches to derive quantitative high-resolution results (exception in Day-Lewis et al. [2003]).

##### 3.1.1. Implementation of the Salt Tracer Simulation

We simulated solute transport using particle tracking and one particle was associated with a certain equivalent additional charge compared to the background charge concentration in the groundwater. If a tracer solution with a lower electrical conductivity than the background groundwater conductivity was injected (desalinated water), particles were associated with a “negative” additional charge. Assuming that the electrical conductivity of the injected tracer solution  $\sigma_{f\_tracer\_injection}$  is constant during the injection and that the background fluid conductivity in the aquifer  $\sigma_{f\_background}$  is constant in space, the electrical conductivity of the fluid at time  $t$  in a grid cell centered at a 3D coordinate  $x$ ,  $\sigma_f(x, t)$ , was related to the number of particles in that grid cell  $n_p(x, t)$  at time  $t$ , the volume  $V_{cell}$  and porosity  $\phi(x)$  in the grid cell, the total number of particles injected  $n_{p\_injection}$ , and the total volume of water that was injected  $V_{injection}$  as:

$$\sigma_f(x, t) = (\sigma_{f\_tracer\_injection} - \sigma_{f\_background}) \cdot C(x, t) / C_{injection} + \sigma_{f\_background} \quad (1)$$

with

$$C(x, t) = n_p(x, t) / (V_{cell} \cdot \phi(x)) \quad (2)$$

and

$$C_{injection} = n_{p\_injection} / V_{injection}. \quad (3)$$

$C(x, t)$  and  $C_{injection}$  are the particle concentrations in a cell and in the injected tracer solution, respectively. Following Müller et al. (2010) we consider a background pore fluid conductivity equal to  $\sigma_{f\_background} = 93.7$  mS/m. For the electrical conductivity of the injected salt tracer, we considered four cases:

1. Injection of water with an electrical conductivity smaller than the background (negative tracer, *Desalinated case*,  $\sigma_{f\_tracer\_injection} = 69.6$  mS/m),
2. Injection with a conductivity slightly higher (positive tracer) than the background (*Low salinity case*:  $\sigma_{f\_tracer\_injection} = 117.8$  mS/m),
3. Injection with an Intermediate conductivity (*Intermediate salinity case*,  $\sigma_{f\_tracer\_injection} = 610$  mS/m), and
4. Injection with a High conductivity (*High salinity case*,  $\sigma_{f\_tracer\_injection} = 1,525$  mS/m)

The *Low salinity case* adds the same magnitude of tracer fluid electrical conductivity as the *Desalinated case* subtracts, and the *High salinity case* adds 2.5 times the tracer fluid conductivity of the *Intermediate salinity case*. The background pore water conductivity and the negative and intermediate tracer conductivities were adopted from the tracer experiments carried out by Müller et al. (2010).

##### 3.1.2. Salt Tracer—Electrical Conductivity Petrophysical Relations

The bulk electrical conductivity  $\sigma_b$  is simplified by an adapted Archie's Law which considers a model of two conductors in parallel: the dissolved ions in the water and adsorbed ions on the soil surface as described by Mualem and Friedman (1991):

$$\sigma_b(x, t) = \sigma_f(x, t)/F(x) + \sigma_{\text{surf}}(x), \quad (4)$$

where  $F(x)$  is the formation factor of saturated soil and  $\sigma_{\text{surf}}(x)$  is the surface conductivity.  $F(x)$  is linked to the complex geometry of the pore channels and is smaller for a larger porosity and smaller tortuosity of the pore network (Archie, 1942; Jackson et al., 1978).  $\sigma_{\text{surf}}(x)$  is controlled by the specific surface area, surface charge density, and effective ionic mobility in the electrical double layer around the charged surface (Johnson et al., 1986). For low fluid conductivities,  $\sigma_{\text{surf}}$  depends in a non-linear way on the fluid conductivity  $\sigma_f$ . But, for sufficiently large  $\sigma_f$ ,  $\sigma_{\text{surf}}$  reaches a constant value so that the relation between  $\sigma_b$  and  $\sigma_f$  is linear (Friedman, 2005), which we assume further in this study.

For  $\sigma_{\text{surf}}$  we based our chosen values on laboratory measurements of soil samples from Krauthausen test site (Müller et al., 2010). Surface conductivities were derived from measurements on sieved material and may therefore be larger than the true values. Therefore, we choose the lowest value observed for the mean  $\sigma_{\text{surf}}$  of 1.2 mS/m to better reflect the presence of stony material in the samples on the electrical conductivity with a standard deviation of 0.3 mS/m. With this information, we generated a random field of  $\sigma_{\text{surf}}(x)$  using SGSIM with the same correlation lengths as  $\sigma_b$  (Table S1 in Supporting Information S1), but with no spatial correlation between  $\sigma_{\text{surf}}$  and  $\sigma_b$  (Müller et al., 2010). Then, we calculated  $F(x)$  using Equation 4 with  $\sigma_f(x, t) = \sigma_{f,\text{background}}$ .

The flowchart in Figure 4 illustrates and summarizes the steps to obtain the tracer concentrations from GPR FWI  $\sigma_b$  images. First,  $F(x)$  is recovered from background GPR FWI  $\sigma_b$  (Figure 4a) using  $\sigma_{f,\text{background}}$  and assuming a constant  $\sigma_{\text{surf}}$ , which represents the average of  $\sigma_{\text{surf}}(x)$  derived from lab measurements. Second,  $\sigma_f$  is estimated from time-lapse GPR FWI  $\sigma_b$  (Figure 4c). Last, the tracer  $\sigma_{f,\text{tracer}}$  is calculated by subtracting  $\sigma_{f,\text{background}}$  from  $\sigma_f$ .

### 3.2. Change in Permittivity and Electrical Conductivity: Ethanol Tracer

Ethanol is commonly used as an additive in gasoline blends (McDowell et al., 2003; Spalding et al., 2011), and is currently treated as an emerging environmental contaminant (Gomez & Alvarez, 2009). The dielectric properties of ethanol differ from water and these differences can be used to detect ethanol in water-saturated conditions in a sand matrix with GPR (Glaser et al., 2012). Pure ethanol has a relative permittivity of 26.7 at 10°C and an electrical conductivity of 0.025 mS/m (Glaser et al., 2012; Petong et al., 2000). Note that the properties of the (ground) water at the Krauthausen test site at 10°C are  $\epsilon_r = 84$  (Malmberg & Maryott, 1956) and  $\sigma \sim 90$  mS/m (Müller et al., 2010). Water-EtOH mixtures are miscible in all proportions as they are both dipolar liquids (Lide, 2004). Ethanol experiences polarization relaxation at central frequency of about 1 GHz and dispersive behavior becomes effective from about  $f > 200$  MHz, lower than those of water: 25 and 1 GHz, respectively (Petong et al., 2000). Thus, dispersive behavior is expected for high GPR frequency ranges, but was not considered in this study using low frequencies between 10 and 200 MHz with central frequency of 57 MHz. Regarding transport properties, ethanol has a lower density and a higher viscosity than water, and it is microbiologically degraded. However, we neglected density, degradation, and temperature effects on ethanol transport for our study, which focused on the ability to retrieve the distribution of the tracer from time-lapse GPR FWI parameter changes ( $\epsilon_r$ ,  $\sigma_b$ ). Therefore, we simulated the ethanol plume migration with the same particle tracking method and using the same transport parameters (velocity, dispersivity) as the ones used for the salt tracer.

#### 3.2.1. Implementation of the Ethanol Tracer Simulation

We produced heterogeneous ethanol plumes that have the same structure as the salt tracer plumes. For the ethanol plume simulations, a particle represents a certain volume of ethanol  $V_{\text{eth}}$ , and therefore the volumetric concentration of ethanol in a cell  $S_{\text{eth}}(x, t)$  is:

$$S_{\text{eth}}(x, t) = S_{\text{eth injection}} \cdot (n_{p \text{ injection}}/V_{\text{injection}})^{-1} \cdot n_p(x, t)/(V_{\text{cell}} \cdot \phi(x)), \quad (5)$$

where  $S_{\text{eth injection}}$  is the volume concentration of ethanol in the injected solution, which was 0.5. The injection volume  $V_{\text{injection}}$  and the duration of the injection were identical to those of the saline tracer simulations.

#### 3.2.2. Ethanol-Permittivity Petrophysical Relations

We derived an effective mixing model for permittivity of water ethanol mixtures,  $\epsilon_{r,p}$  at 10°C by fitting a second-order polynomial to experimental data (Wyman, 1931):

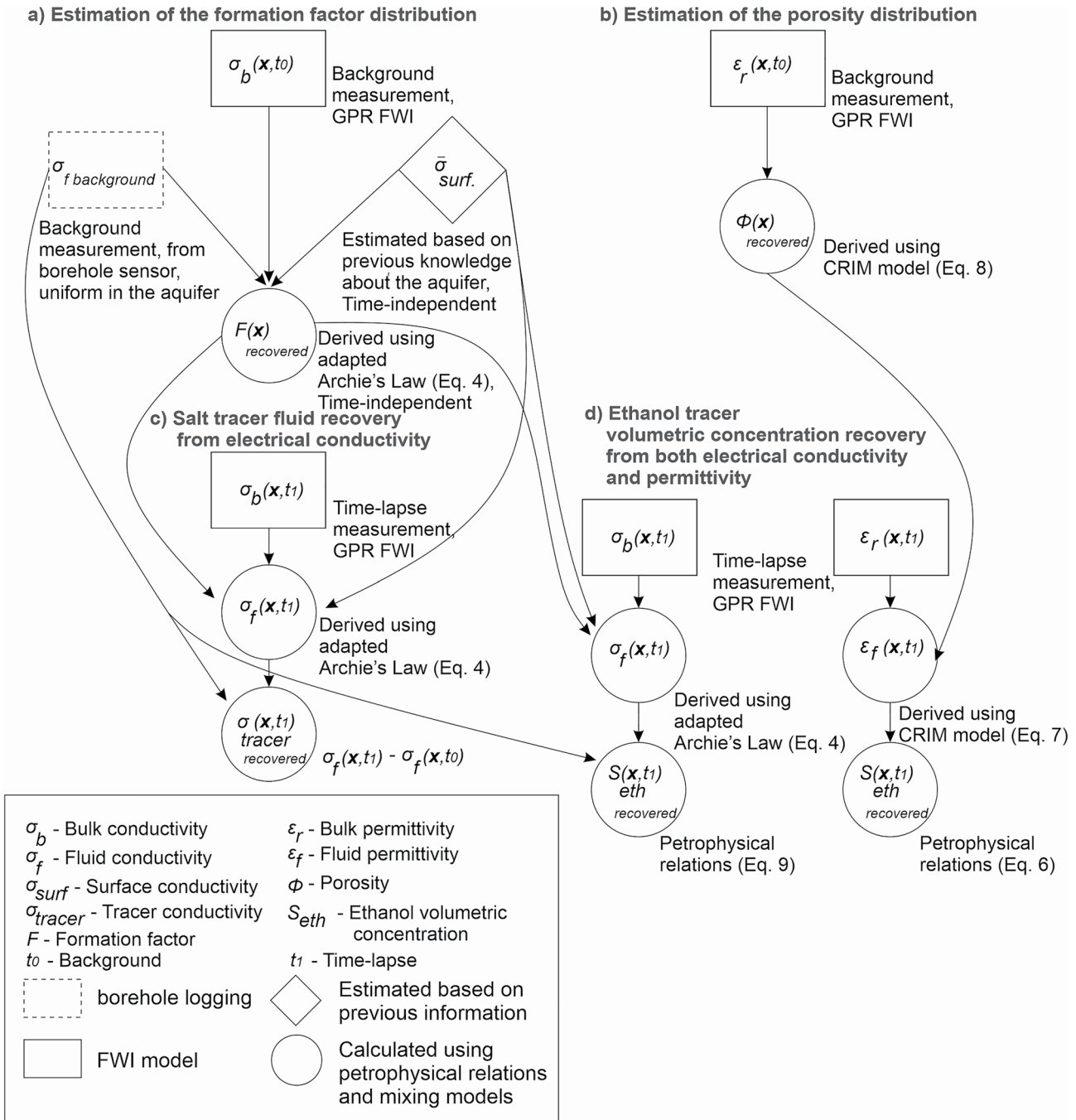


**Figure 4.** Flowchart presenting the recovery of solute (salt and desalinated water) and ethanol tracers. (a) Formation factor and (b) porosity recovery from background ground penetrating radar (GPR) full-waveform inversion (FWI). (c) Salt and (d) ethanol recovery from time-lapse GPR FWI.

$$\epsilon_{r,f}(x, t) = 84.05 - 42.6 \cdot S_{eth}(x, t) - 15.7 \cdot S_{eth}(x, t)^2 \quad (6)$$

To derive the bulk relative permittivity  $\epsilon_r$  of the mixture-soil system, we used the Complex Refractive Index Model (CRIM) (Birchak et al., 1974)

$$\epsilon_r(x, t) = (\phi(x)\sqrt{\epsilon_{r,f}(x, t)} + (1 - \phi(x))\sqrt{\epsilon_{r,s}})^2 \quad (7)$$



where  $\epsilon_{r,s} = 4.5$  is the relative permittivity of the solid grains (Carmichael, 1988). In order to retrieve  $\epsilon_{r,f}$  and eventually  $S(x,t)$  from a GPR FWI permittivity model (Figure 4d), the porosity must be recovered from  $\epsilon_r$  background measurements (Figure 4b):

$$\phi_{\text{recovered}}(x) = (\sqrt{\epsilon_r(x, t_0)} - \sqrt{\epsilon_{r,s}}) / (\sqrt{\epsilon_{r,f}} - \sqrt{\epsilon_{r,s}}) \quad (8)$$

### 3.2.3. Ethanol-Conductivity Petrophysical Relations

We modeled the electrical conductivity of the ethanol-water fluid mixture following Personna et al. (2013):

$$\sigma_f(x, t) = (S_{\text{eth}}(x, t) \cdot \sigma_{\text{eth}}^\alpha + (1 - S_{\text{eth}}(x, t)) \cdot \sigma_{f,\text{background}}^\alpha)^{1/\alpha} \quad (9)$$

where  $\sigma_{\text{eth}} = 0.0252$  mS/m is the ethanol electrical conductivity, with  $\alpha = 0.3$  for ethanol volumetric concentration  $S_{\text{eth}} \leq 0.5$ .

In order to retrieve  $\sigma_f(x,t)$  and eventually  $S_{\text{eth}}(x,t)$  from a GPR FWI bulk electrical conductivity model (Figure 4c), the formation factor must be recovered from  $\sigma_b(x,t_0)$  background measurements (Figure 4a, Equation 2).

## 4. GPR FWI Modeling

Generally, the time-domain crosshole GPR FWI is an iterative approach that simultaneously estimates  $\epsilon_r$  and  $\sigma_b$  by minimizing the misfit function between measured and modeled GPR data with a gradient-type approach (for more details we refer to Meles et al. [2010] and Klotzsche, Vereecken, and van der Kruk [2019]). Thereby, a 2D finite-difference time-domain algorithm is used that solves the full Maxwell equations and allows predicting the EM wave propagation through the heterogeneous medium. To prevent the misfit function from converging to a local minimum, a  $\epsilon_r$  starting model is required that yields synthetic traces that match all the observed data within less than half of the wavelength to avoid cycle-skipping (Meles et al., 2010). Normally, ray-based inversion results can provide such starting models. In the presence of high contrasts, such as a water table or high permittivity zones, ray-based starting models often need to be updated to meet these criteria (Klotzsche et al., 2012). Local invasion of tracer may generate high contrasts in  $\epsilon_r$  and  $\sigma_b$  over short distances, which cannot be resolved by ray-based inversions and could cause problems in the FWI by using ray-based inversions as starting models. Therefore, we need to evaluate different starting model strategies for the time-lapse approach to guarantee that the half-wavelength criterion is always fulfilled in the entire domain of investigation. So far, most studies analyzed the effect of starting model errors mainly on the  $\epsilon_r$  model and different methods were suggested, such as the amplitude analysis approach, to guarantee meeting the wavelength criterion (e.g., Klotzsche et al., 2014; Zhou et al., 2020). The definition of the  $\sigma_b$  starting model is more challenging. Although the first cycle amplitude inversion provides a first guess for a homogenous starting model (e.g., Klotzsche et al., 2010), we need to investigate in more detail how to best handle the  $\sigma_b$  starting model for high contrast time-lapse changes.

Synthetic GPR data were calculated using the highly resolved parameters of the aquifer model in a crosshole setup at 10 m distance from the injection borehole and perpendicular to the main flow direction (Figures 2, 3a, and 3b). The distance between the boreholes was 4.95 m. GPR data were derived below the water table (2.4 m depth) between 3.2 and 10 m depth. We added a realistic random instrumental noise level to the synthetic traces to evaluate its effect on the inversion performance (Figure S1 in Supporting Information S1). To realistically include reflection and refractions of the GPR data, we describe the unsaturated zone above 2.4 m depth with  $\epsilon_r = 8$  (in the range of  $\epsilon_r$  for “soil sandy dry” in Table 4.1 in Daniels [2004]). Similar to previously performed GPR measurements at the Krauthausen test site (Oberröhrmann et al., 2013), we used a semi-reciprocal acquisition setup with 35 transmitters and 69 receivers on each side, spaced with 0.2 and 0.1 m, respectively. With this setup a high ray coverage that enhances the electrical conductivity reconstruction can be obtained (Keskinen et al., 2021). We considered for our modeling a constant source wavelet (SW) with a central frequency of 57 MHz for the background and time-lapse cases (adopted from a previous FWI studies [Gueting et al., 2015, 2020]). It has been shown in experimental studies that for this operating frequency GPR FWI models can be obtained with a vertical resolution as small as 0.2 m (Zhou et al., 2020). Note that changes on the effective wavelet caused by the difference in borehole filling caused by the tracers are not considered in this study, and will be investigated for the experimental data applications.

In this numerical study, we concentrate on modeling and inverting 2D data, because of the high computational demanding 3D environment (detailed discussion in Section 6.1 and Text S4 in Supporting Information S1). For the inversion and forward modeling, we considered a model cell size of 0.09 and 0.03 m, respectively. Note that the inversion grid has the same cell size as the transport simulation (Figure 3b). To avoid numerical artifacts in the crosshole GPR FWI that are caused by high gradients of the  $\epsilon_r$  and  $\sigma_b$  near the boreholes, we considered the approach based on van der Kruk et al. (2015) that allows an update of the medium properties close to the boreholes by using a gradient preconditioning. The criteria for choosing the final iteration and to stop the inversion of the time-lapse data sets is based on Klotzsche, Vereecken, and van der Kruk (2019):

1. the root-mean-squared error (RMSE) of the observed and modeled data between subsequent iterations changes less than 0.5%,
2. decrease of at least 50% in RMSE in contrast to the ray-based inversion starting model,
3. absence of the remaining gradients (in the FWI optimization method) for the final models, and
4. good fit between the measured and modeled data (direct sample by sample correlation without any shift should be better than 0.8). Note that this value indicates a good trend in the data fit and is based on experimental data experience.

It is important to note that all four points need to be satisfied. For example, if the data fit is less good, although maybe the other three points are satisfied, it indicates that a model was found which is not providing data that fit the entire measured data range (Klotzsche et al., 2014).

## 5. GPR FWI Results

### 5.1. Background Models

To evaluate tracer changes over time, we derived FWI results for background data, measured before a tracer injection. The starting models for this FWI were derived from ray-based inversion results (Figures 5b and 5g). For the  $\sigma_b$  starting model, we considered a uniform  $\sigma_b$  of 15 mS/m provided by the mean of the first-cycle amplitude inversion and adaptations of this value based on numerical forward modeling tests (Holliger et al., 2001). In contrast to the ray-based inversion results, the FWI results better reconstruct the medium parameters and resolve finer structures, which the ray-based inversion is not able to detect (Figure 5b). Additionally, we performed the FWI for the noise-free and noise-added data sets (Figures 5c, 5d, 5h, and 5i). Both  $\epsilon_r$  and  $\sigma_b$  results show the same structures with decimeter-scale resolution for the noise-free and noise-added data sets. The final RMSE of the noise-added and the reconstruction of the parameters is only slightly less good in comparison to the noise-free data (Table S2 in Supporting Information S1). The minor differences are caused because the noise-added data set inversion cannot fit the data below the noise level. Since we have seen that the FWI models of both data sets reconstruct almost identical parameters, hereafter we consider only the more realistic noise-added data set.

Generally, the reconstruction of the permittivity and conductivity is very good by the FWI, which is also indicated by the lower RMSE of the modeled data, the FWI data correlation coefficient of almost 1, and the low FWI  $\epsilon_r$  and  $\sigma_b$  model errors compared to the real models (Figures 5e and 5j; Table S2 in Supporting Information S1). It can be noticed that the model errors are larger at locations of high contrasts. The RMSE of the background models are 0.86 for  $\epsilon_r$  and 1.64 mS/m for  $\sigma_b$ . The  $\epsilon_r$  FWI models resolved the fine features better than the FWI  $\sigma_b$  models, as indicated in horizontal and vertical 1D profiles and by spectral analysis (Figure 6, Van der Schaaf & van Hateren, 1996). The illumination of the domain using crosshole acquisition results in a better resolution of the vertical than the horizontal structures (Meles et al., 2010). In the vertical direction, the ratio of the spectral densities of the FWI to the real model starts decreasing for wavenumbers larger than  $\nu = 3 \text{ m}^{-1}$  and  $\nu = 1.13 \text{ m}^{-1}$  (equivalent to wavelength  $\lambda$  of 0.33 and 0.88 m,  $\lambda = 1/\nu$ ) for  $\epsilon_r$  and  $\sigma_b$ , respectively. In the horizontal direction, this ratio starts decreasing for wavenumbers larger than  $\nu = 0.77 \text{ m}^{-1}$  ( $\lambda = 1.3 \text{ m}$ ) and  $\nu = 0.51 \text{ m}^{-1}$  ( $\lambda = 2 \text{ m}$ ) for  $\epsilon_r$  and  $\sigma_b$ , respectively.

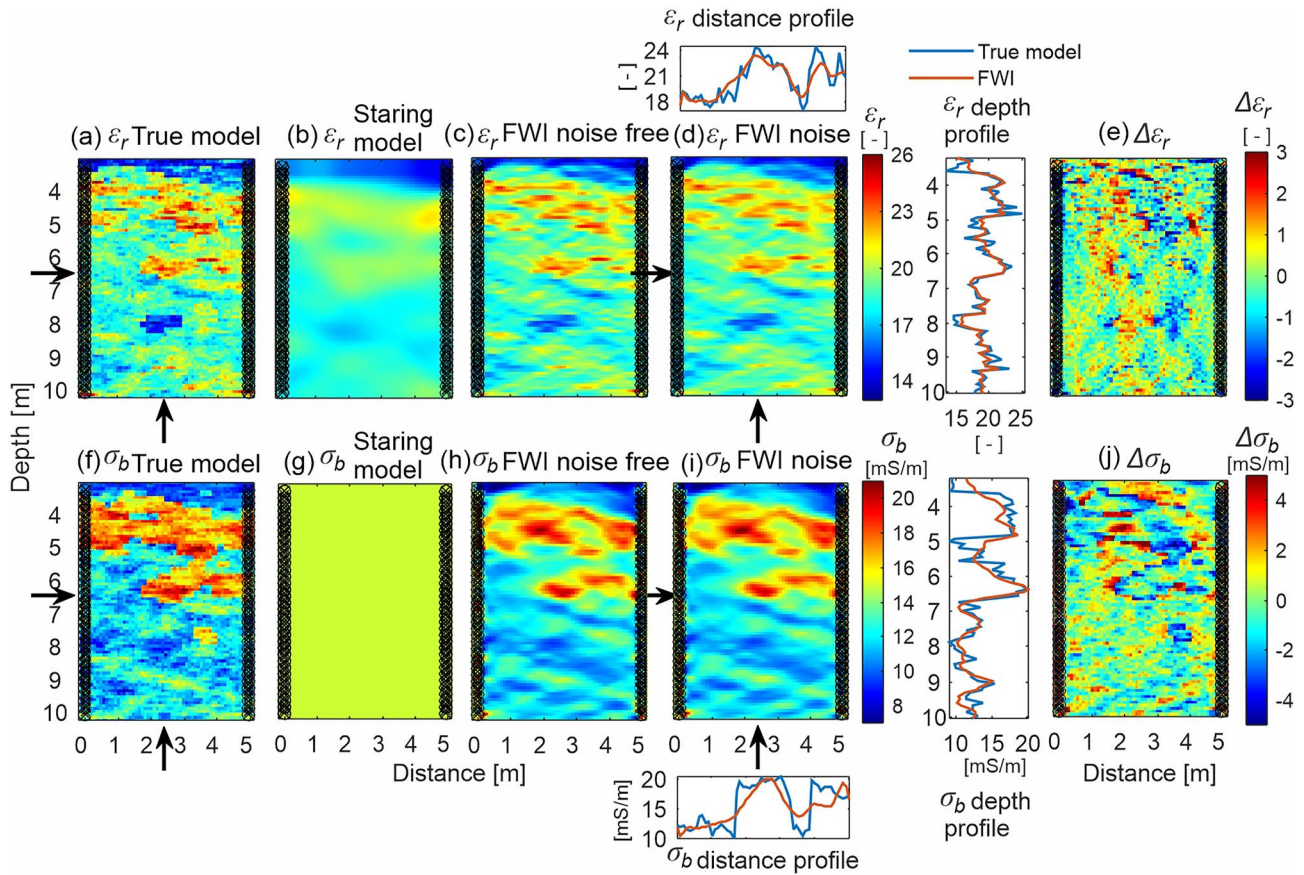


**Figure 5.** Background permittivity (top row) and electrical conductivity (bottom) models. (a and f) Real models, (b and g) starting models based on ray-based inversion results, and (c and h) full-waveform inversion (FWI) models of the noise free data set and (d and i) with noise. Panels (e and j) show the difference between real and FWI models with noise. Transmitter and receiver positions are located on black circles and crosses, respectively near the panel side boundaries. Above and right to (d), plots compare the real (blue) with FWI (orange) permittivity models (a and d) along vertical profile at 2.5 m distance and horizontal profile along 6.5 m depth (indicated by arrows). Below and right to (i), plots compare the real (blue) with FWI (orange) electrical conductivity models (f and i).

## 5.2. Porosity and Formation Factor Estimation of the Background Models

Calculating the porosity  $\phi_{\text{recovered}}$  and the formation factor  $F_{\text{recovered}}$  distributions using Equations 4 and 8 (Figure 7) for both background ray-based and FWI results (Figures 5b, 5d, and 5i), we can see clearly that FWI better reconstructs the parameters than the ray-based inversion. The  $\phi_{\text{recovered}}$  calculated from ray-based shows smoothed and dampened structures, while the FWI  $\phi_{\text{recovered}}$  structures show more details and are closer to the true model  $\phi_{\text{RM}}$  (Figures 7a–7c). The  $F_{\text{recovered}}$  calculated from the ray-based (attenuation) inversion recovered an erroneously lower value and a smaller variance than in FWI (Figures 7e–7g). Thus, FWI provides a more accurate recovery than the ray-based inversion of these parameters, which in turn, through the use of petrophysical relations, reduces the uncertainty of the tracer recovery.  $\phi_{\text{recovered}}$  shows a better correlation with  $\phi_{\text{RM}}$  than  $F_{\text{recovered}}$  with the true model  $F_{\text{RM}}$ . The mismatch for both parameters is related to the unresolved structures and deviations between FWI and real  $\epsilon_r$  and  $\sigma_b$  models (Table S2 in Supporting Information S1, Figures 5e and 5i). Low values of  $\phi_{\text{recovered}}$  ( $<0.28$ ) overestimate  $\phi_{\text{RM}}$ , while high values of  $\phi_{\text{recovered}}$  underestimate  $\phi_{\text{RM}}$  (Figure 7c), which is a bias originating from FWI results. We derived  $F_{\text{RM}}$  using the  $\sigma_{b,\text{background}}$  from a previous study by Gueting et al. (2015, 2020). Note that this  $F$  is larger than the point measurements of Müller et al. (2010), where the soil was sieved and only soil grains smaller than 20 mm were considered. For higher values of  $F_{\text{recovered}}$  ( $>10$ ) we can notice larger scatter. Locations with a high  $F$  correspond with locations where  $\sigma_{b,\text{background}}$  is low. Errors in the recovered  $\sigma_{b,\text{background}}$  and deviations between the local  $\sigma_{\text{surf}}$  and the mean  $\sigma_{\text{surf}}$ , which is used to recover  $F$ , lead to a larger scatter for high values of  $F_{\text{recovered}}$ .

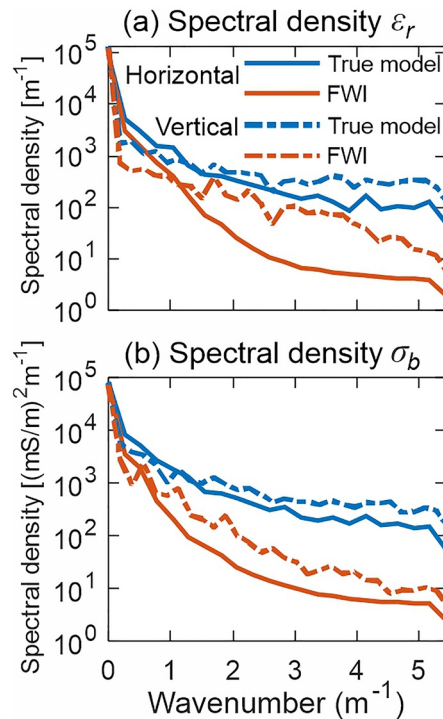


**Figure 6.** Spectral density of (a) permittivity and (b) electrical conductivity. Curves compare between the real models (RM, blue) and reconstructed full-waveform inversion (orange) models for horizontal (solid line) and vertical (dashed line) directions.

Analyzing the correlation plots between the true and the FWI recovered distribution of  $F(x)$  shows a range from 4.5 to 14.5.  $F$  is bimodally distributed (Figure 7d), reflecting the two main facies 1 and 2 (Figure 3a, whereas the contribution of Facies 3 is minor). The sand facies 1 has a mean porosity of  $\phi_{1\_mean} = 0.36$  and a mean  $F(x)$  of approximately 6. The sandy gravel facies 2 shows a mean porosity  $\phi_{2\_mean} = 0.31$  and a mean formation factor of 8.5. The gravel facies 3 has a mean porosity  $\phi_{3\_mean} = 0.25$  and a mean  $F(x)$  value is about 11, which is larger than the laboratory measured value for the disturbed samples of Müller et al. (2010) of 4.56–6.63, which excluded larger stones.

### 5.3. Starting Model Strategies for Time-Lapse FWI

As mentioned before, for the FWI of time-lapse data it is highly important to guarantee that the starting models of the different time steps hold the half wavelength criterion. Because of the extensive knowledge that is already existing on how to optimize the  $\epsilon_r$  starting model (e.g., Keskinen et al., 2021), we will concentrate on defining the best strategy for time-lapse  $\sigma_b$  starting models, which to our knowledge has not been investigated before.

Therefore, we first tested four different FWI starting model strategies for the salt tracer time-lapse GPR data. Note that we used for all the strategies the FWI  $\epsilon_r$  background model  $m_0$  as permittivity starting model, while for the  $\sigma_b$  starting model different options were tested: using a uniform  $\sigma_b$  value (FWI1), the background model  $m_0$  (FWI2) and the previous day model  $m_{t-1}$  (FWI3, FWI4). For FWI3 the  $m_{t-1}$  model was calculated from the day-by-day sequential FWI inversions starting with the background, while in FWI4  $m_{t-1}$  was calculated using a single FWI inversion with starting model  $m_0$ . Note that we also tested different standard ray-based starting model approaches for the permittivity, which resulted in less good results and reconstructions of the tomograms, and we therefore do not present them.

For all the tests, the real permittivity models are unchanged (Sreenivas et al., 1995) in the salt tracer test and therefore only the  $\sigma_b$  real models are investigated.

For the FWI starting model tests (Figure 8), the time-lapse GPR data are derived for day 15 after the salt tracer injection based on the  $\sigma_b$  distribution shown in Figure 8a. Overall, all the 4 FWI recovered the main structures of the true model. While FWI1 shows fewer features of the tracer anomaly, FWI2 provided more accurate structures and performs better based on  $R^2$  between the true and FWI model and the RMSE of the difference between the two ( $R^2 = 0.64, 0.66, 0.58, 0.69$ ; RMSE [mS/m] = 5.8, 5.6, 6.5, 5.4 for FWI strategies 1–4, respectively). Although FWI3 provides a more detailed  $\sigma_b$  structure, the  $R^2$  and the RMSE of FWI3 compared to the true model resulted in a worse performance than of FWI1 and FWI2. Analyzing the spectral density in the recovered FWI  $\sigma_b$  models (Figure 9), FWI3 provides the most information. These results of FWI3 are explained on the one hand by a better resolution of small-scale structures due to the better  $\sigma_b$  starting model from the previous day  $m_{t-1}$ , but on the other hand there is a lower accuracy due to model overfitting, most likely caused by accumulation of errors in recovered FWI models which are then used as starting models for the following day.

The structure of FWI4 is similar to FWI2 but does not show as many details as FWI3. The best results of the four different starting models are obtained with FWI4, while the spectral analysis information is between FWI3 and FWI2. Overall, FWI2 shows robust results and in addition can be applied fast, because as a starting model it requires the FWI background and not any following day.

Thus, all FWI from here (for both salt and ethanol tracer tests) will use FWI2 starting model strategy.



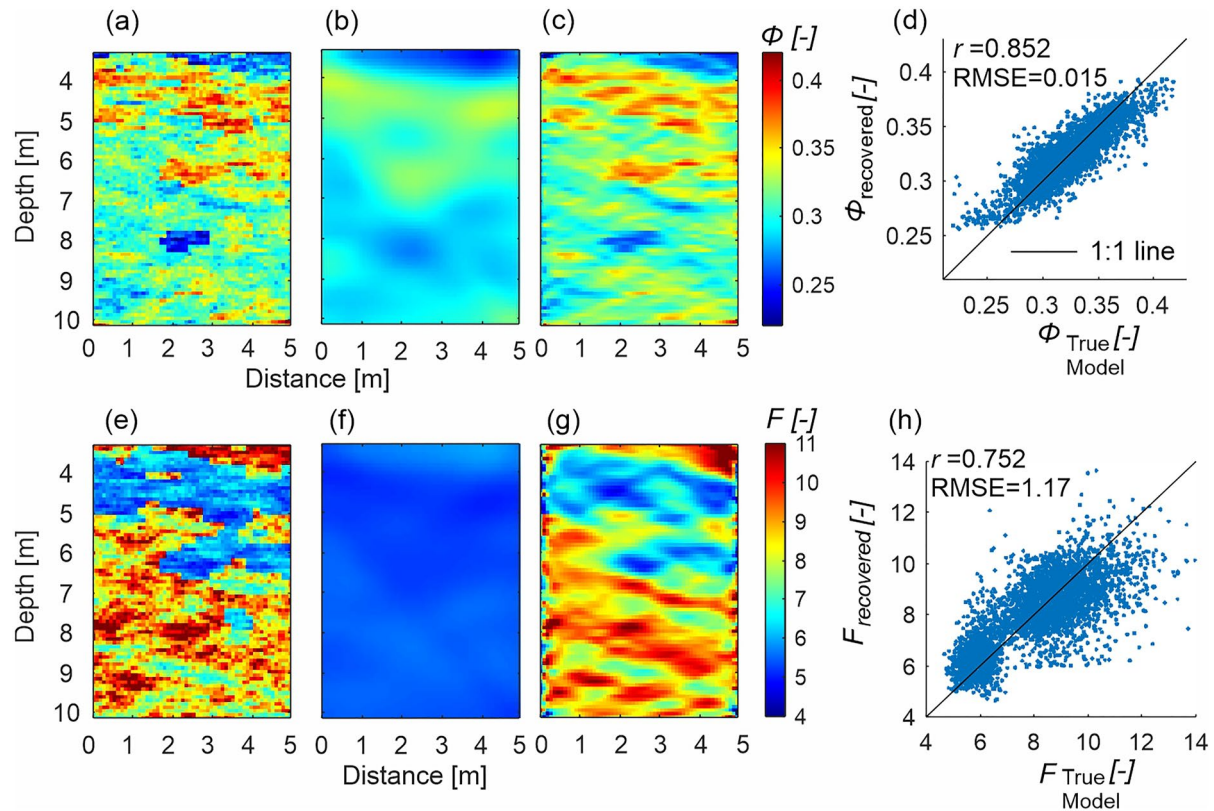


**Figure 7.** Porosity (top row) and formation factor (bottom row) distribution calculated from permittivity and electrical conductivity models, respectively: (a and e) show the true models, (b and f) are calculated from the ray-based models, and (c and g) from the full-waveform inversion (FWI) models. (d and h) Correlation plots between the true and FWI recovered (d) porosity and (h) formations factors.

#### 5.4. Recovery of Different Salt Tracer Magnitudes and Days

After we defined an appropriate starting model strategy, we now apply this to four different salt tracer scenarios with different  $\sigma_b$  changes at day 15 after injection. Similar to the tests before, the real permittivity models are unchanged for all scenarios and only the  $\sigma_b$  models are analyzed (Figure 10).

For injections with *Intermediate* and *High* salinity tracers, the  $\sigma_b$  distribution is predominantly determined by the distribution of the saline tracers, which generate larger variations in  $\sigma_b$  than the spatial variations of  $\sigma_{b,\text{background}}$  (Figures 10d and 10e). For the *Desalinated* (negative) and *Low salinity* (positive) tracers, the changes in  $\sigma_b$

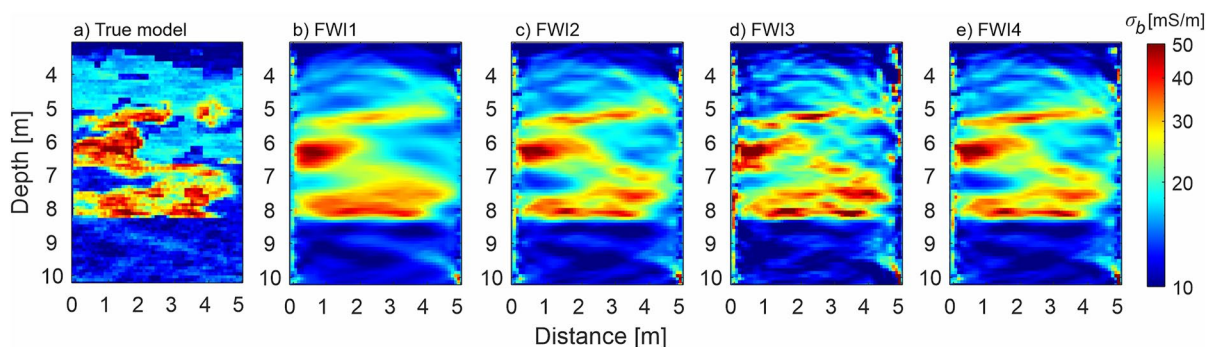


**Figure 8.** Full-waveform inversion (FWI)  $\sigma_b$  results for the salt tracer using different starting model strategies. (a)  $\sigma_b$  true model at day 15. (b–e) FWI  $\sigma_b$  models from using starting models' strategies FWI 1–4, as explained in the text.

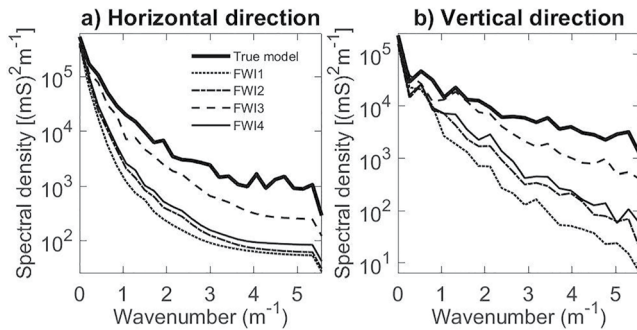


**Figure 9.** Spectral density of recovered full-waveform inversion (FWI)  $\sigma_b$  using different starting model strategies. The spectral information of the true model is shown by a thick line, and of the FWI from different starting model strategies by thinner curves. FWI 1–4 are presented in Section 5.3. (a and b) Spectral density in horizontal (solid line) and vertical (dashed line) directions, respectively.

are in the same order of magnitude as the spatial variation in  $\sigma_{b, \text{background}}$  (Figures 10a–10c). The FWI  $\sigma_b$  models show a recovery of the structures for all cases, but the *High-salinity* case shows a worse recovery, for example, at  $z = 6.5$  m,  $x = 1$  m it misses a main anomaly, probably due to the high attenuation of the signal.

Investigating the data fit between the simulated and FWI modeled traces between 4 and 8 m (Figure 11, Figure S2 in Supporting Information S1 for *Desalinated* and *High salinity* cases) for the different salinity cases of day 15 (Figure 10), we generally notice a good overlap of the traces and that FWI traces can recover most details of the traces. A higher  $\sigma_b$  entails lower amplitudes causing gradually decreased amplitudes from Background to *Intermediate salinity* cases (Figures 11a–11c, compare the *Observed* data for the transmitter shot gathers at 6 m of different cases—note for the amplitude scale). We observed a gradual decrease in  $R^2$  between the true and modeled traces from Background to *Intermediate salinity* cases. The FWI traces seem to have difficulties to fit the signal amplitude and phase at regions where the tracer intrudes in comparison to where there is no intrusion (e.g., between transmitter at 6 and 9.6 m in *Intermediate salinity* case). This is even more

pronounced for the *High salinity* case (Figure S2b in Supporting Information S1). At the central part of the plume, the *High salinity* FWI traces at 6 and 7 m show a bad fit (Figures S3f and S3h in Supporting Information S1), with erroneous amplitudes and phase shifts.

Note, at high salinities the amplitudes of traces that cross regions with tracer intrusion are much lower than those of traces that cross regions without tracer intrusion and can be even lower than the instrumental noise level (Figure S4b in Supporting Information S1). No weighting on the data is applied to enhance the small residuals and for all data the squared differences between the measured and modeled traces are minimized. As a consequence, a poor match is obtained between the measured and FWI modeled traces for the high salinity data having much lower amplitude (Figures S3f and S3h in Supporting Information S1). The higher conductivity changes

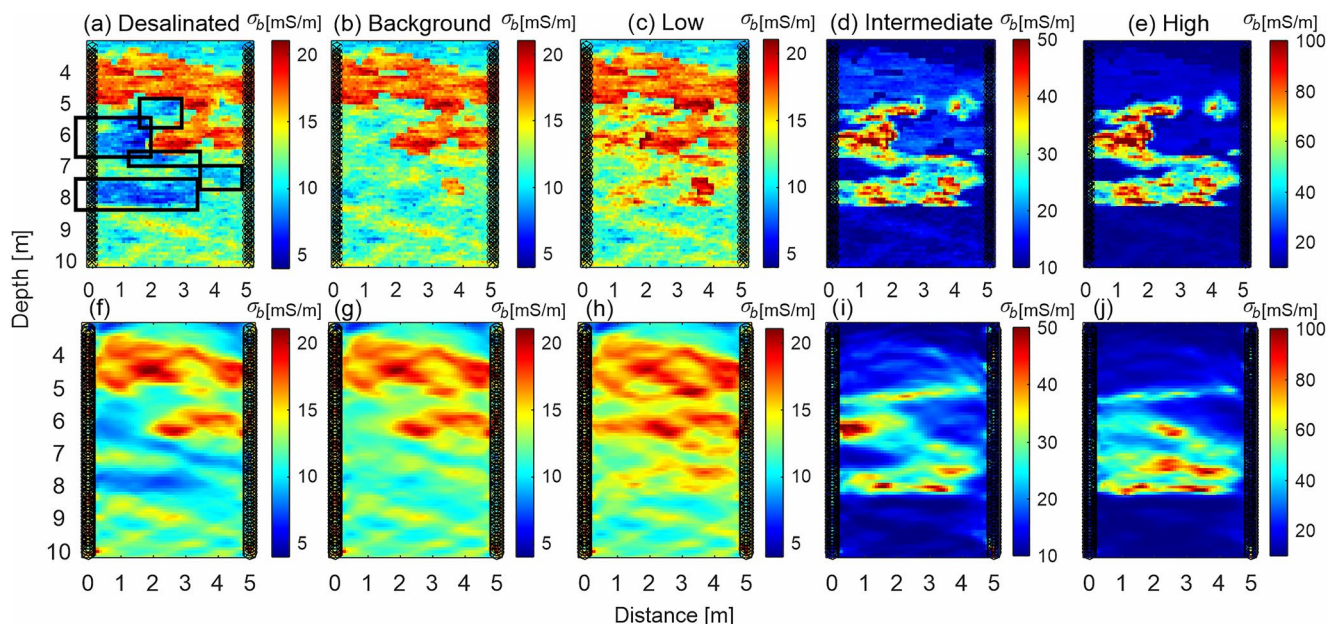


**Figure 10.** Bulk electrical conductivity full-waveform inversion recovery from the synthetic salt tracer. Input (top) and recovered (bottom) models in the monitoring plane for different cases of injected salt tracer salinities: (a and f) Desalinated water, (b and g) Background, (c and h) Low, (d and i) Intermediate and, (e and j) High. The intrusion is shown for 15 days after the injection, and the main location of the tracer intrusion are emphasized by rectangles in (a). Note that panels (a–c and f–h) have the same colorbar scale, and (d–e and i–j) have different ones. Transmitter and receiver positions are located on black circles and crosses, respectively near the panel side boundaries.



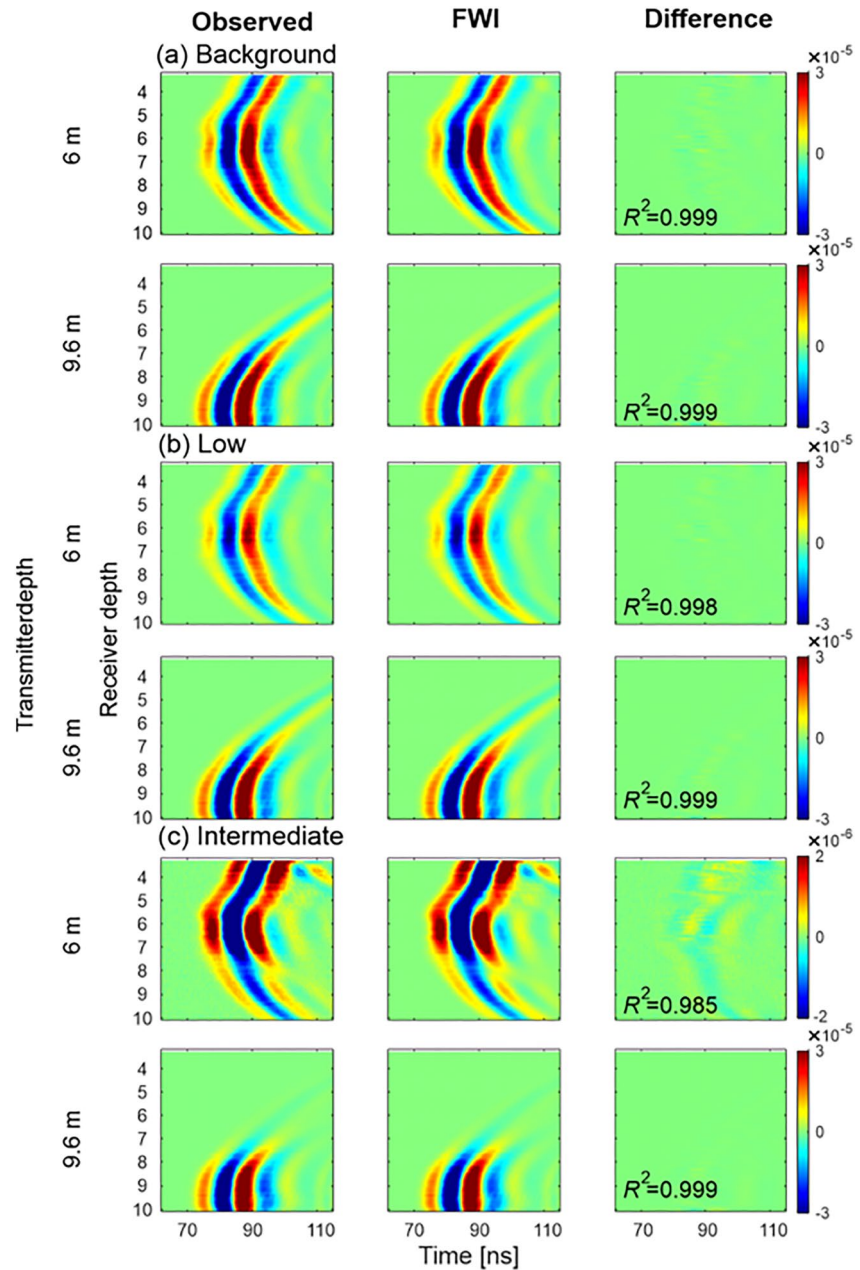


**Figure 11.** Observed (real data noise-added), full-waveform inversion (FWI) inverted and the difference between inverted and observed data for transmitters at the depth of major tracer intrusion (6 m) and at depth, where no intrusion occurs (9.6 m). GPR Data is presented for the (a) background (tracer case in Figure 9b) and (b and c) *Low* and *Intermediate* (tracer case in Figures 9c and 9d) salinity tracer cases. Note that for the *Intermediate* salinity case in (c) for the transmitter at 6 m depth panel where the signal is weaker because the wave travels through the increased  $\sigma$  of the tracer, the color scale is 15 times smaller.  $R^2$  quantifies the correlation between FWI inverted and the observed data. The standard deviation of the Gaussian random noise was  $4.6 \times 10^{-8}$  in all cases. *Desalinated* and *High* salinity cases are shown in Figure S2 of Supporting Information S1.

result in an increased non-linearity of the FWI, which is more difficult to invert and needs more sophisticated FWI techniques using progressively expanded bandwidths of the data and effective SW (Zhou et al., 2021), which are beyond the scope of this paper.

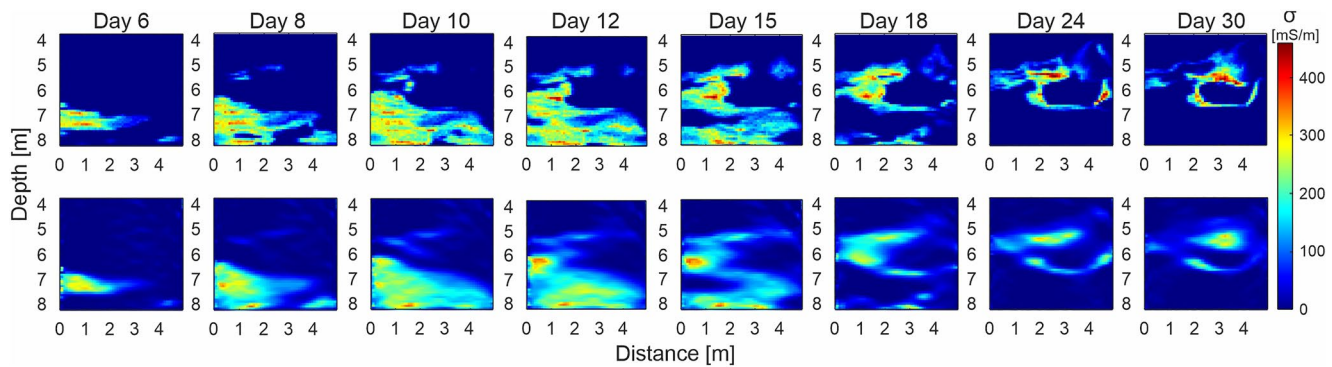


**Figure 12.** Salt tracer conductivity  $\sigma_r$  recovered on different days. Top row: real  $\sigma_r$  from transport simulation. Bottom row: recovered  $\sigma_r$  from ground penetrating radar full-waveform inversion bulk conductivity. Only the depths within the transport model domain are shown, from 3.67 to 8.26 m.

To evaluate the possibility to monitor the  $\sigma_r$  tracer movement and transport over time, we performed an intense study by inverting 50 sequential days for the *Intermediate-salinity* case (Figure 12, 8 days chosen from day 6 until day 30). At all days the structures of the plume could be recovered and resolved to about 0.2 m scale, thus showing the potential of time-lapse monitoring.

### 5.5. Recovery of Ethanol Tracer

As described in Section 3.2, we derived GPR data for a synthetic ethanol tracer experiment. Similar to the saline tracer tests, we considered the distribution of the tracer at day 15 after the tracer injection and applied for the  $\sigma_b$  starting model the optimal strategy by considering the background FWI results. To define the optimal  $\epsilon_r$  starting model for this time-lapse data, we performed different tests by considering the travel time inversion (not shown) and the FWI results of the background data. As expected, the background FWI model provided the best results, therefore we choose this strategy for the following steps and do not show the FWI results for other tests.

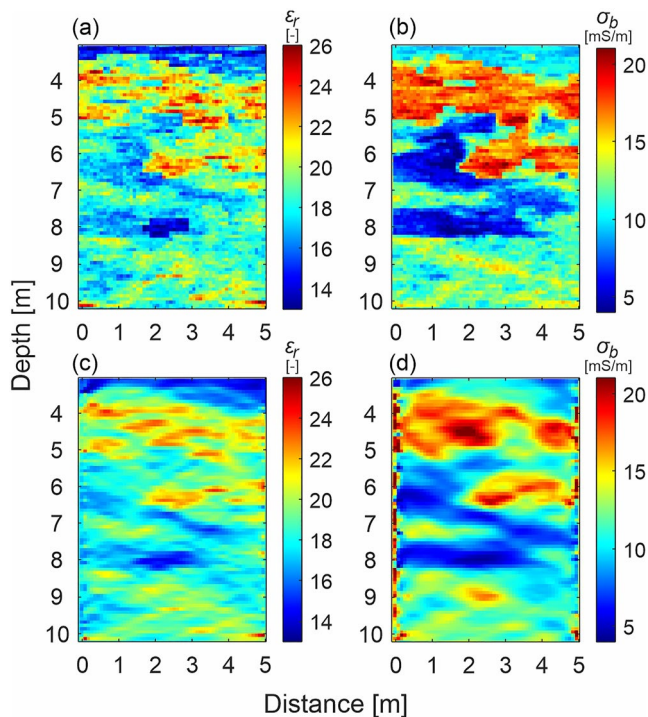


**Figure 13.** Permittivity and bulk electrical conductivity full-waveform inversion (FWI) recoveries from the synthetic ethanol tracer for 15 days after the injection. Real models are shown in (a) permittivity and (b) electrical conductivity, while (c and d) show the corresponding FWI results.

The true models of  $\epsilon_r$  and  $\sigma_b$  in the monitoring plane 15 days after the ethanol tracer injection show a decrease in both  $\epsilon_r$  and  $\sigma_b$  (Figures 13a and 13b) compared with the background (Figures 5a and 5e), with maximum changes of  $\Delta\epsilon_r = -3.35$  and  $\Delta\sigma_b = -11.95$  mS/m at  $Z = 6.3$  m,  $X = 1$  m. This corresponds to the GPR traces with increased amplitude, and which are shifted to earlier times by about 1–1.5 ns (examples of ethanol FWI and corresponding real traces at the main intrusion depth are shown in Figure S5 of Supporting Information S1). We used the FWI results of the background as a starting model (Starting model strategy FWI2). Overall, both medium parameters are resolved well, and the main features are detected within high resolution. Especially permittivity changes caused by the ethanol tracers around 8 m depth are well reconstructed. The final FWI  $\sigma_b$  recovery is more smoothed than the  $\epsilon_r$  recovery (Figures 13c and 13d), as was also observed for the FWI background models (Figure 5). This phenomenon is related to a higher sensitivity in  $\epsilon_r$  in fitting the phase than in fitting the amplitude of the signal in natural media (Lavoué et al., 2015). Modeled FWI traces (blue dashed lines in Figure S5 of Supporting Information S1) for the ethanol case show a good fit to the observed traces.

Also, for the ethanol tracer, we performed a similar study as for the *Intermediate* salinity case and calculated for 50 consecutive days the FWI results using starting model strategy FWI2 (Figure 14). For these days, we recovered the volumetric concentration of ethanol  $S_{eth}$  distributions from time-lapse



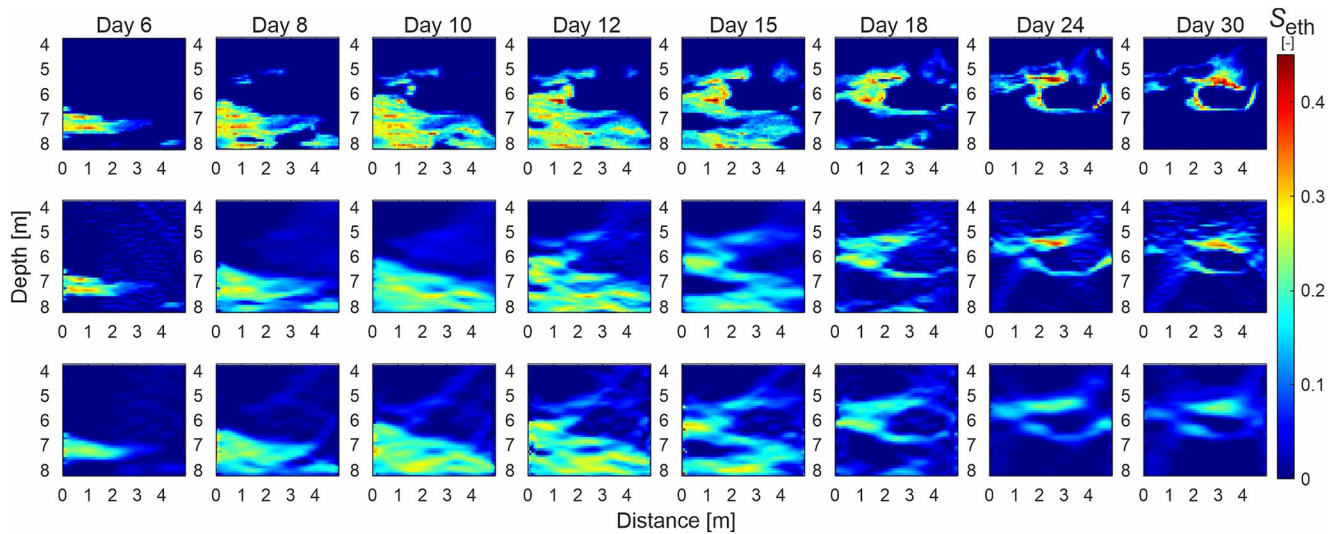


**Figure 14.** Volumetric concentration of ethanol  $S_{eth}$  recovered on different days. Top row: real  $S_{eth}$  derived from transport simulation. Middle and bottom rows: recovered  $S_{eth}$  from ground penetrating radar full-waveform inversion permittivity and conductivity, respectively.

FWI  $\epsilon_r$  and  $\sigma_b$  models. For both cases, the  $S_{eth}$  distributions show a good correspondence to the true time-lapse distributions for all days. Because of the better recovery of FWI  $\epsilon_r$  (see also Figure 13), a more accurate recovery of  $S_{eth}$  distribution is derived from  $\epsilon_r$  than from  $\sigma_b$ , which is also caused by higher uncertainty in  $\sigma_{surf}(x)$  that propagates in the derivation of  $S_{eth}$  from  $\sigma_b$ . In addition, since the uncertainty of  $\phi_{recovered}$  is smaller than that of  $F_{recovered}$  (Figure 7), less errors propagate in the recovery of  $S_{eth}$  from  $\epsilon_r$  than from  $\sigma_b$ .

Further, subtracting  $\epsilon_r$  at day 13 from that in day 15 (Figures 15a and 15b) shows that time-lapse GPR FWI can image tracer changes based on time lapse  $\epsilon_r$  images with about 0.2 m resolution, and better than from time lapse  $\sigma_b$  images (Figures 15c and 15d).

Movie S1 shows the tracer reconstruction and developments over time for both ethanol and salt tracers can be found in a link to be provided. Description is given in Text S3 of Supporting Information S1.

### 5.6. Breakthrough Curves at Single Cells

The day-by-day tracer FWI recovery results of the *Intermediate-salinity* and the ethanol tracer allowed to calculate the breakthrough curves (BTC) at each single cell (0.09 m) in the crosshole tomogram. From these results three FWI parameters can be considered:  $\sigma_b$  from salt tracer (Figure 16a), and  $\epsilon_r$  and  $\sigma_b$  from ethanol tracer (Figure 16b). The true tracer properties ( $\sigma_r$  or  $S_{eth}$ ), which were derived using petrophysical relations from the same synthetic transport simulation, were normalized to the highest values, to allow a better comparison. From observing BTCs at four random locations (Figures 16a and 16b) we identify that the shapes of the FWI breakthrough curves are in general recovered. However, for the majority of the recovered BTCs the first arrival is too early, the tail is too long, and the breakthrough peak is in general too low, but sometimes also too high. That inaccuracy is partly because for the given acquisition settings the receiver antenna records a signal which represents roughly the volume of the wave path with an effective cross-section of the size of Fresnel zone and with a diameter of about 1.25 m (in Section 6.1).

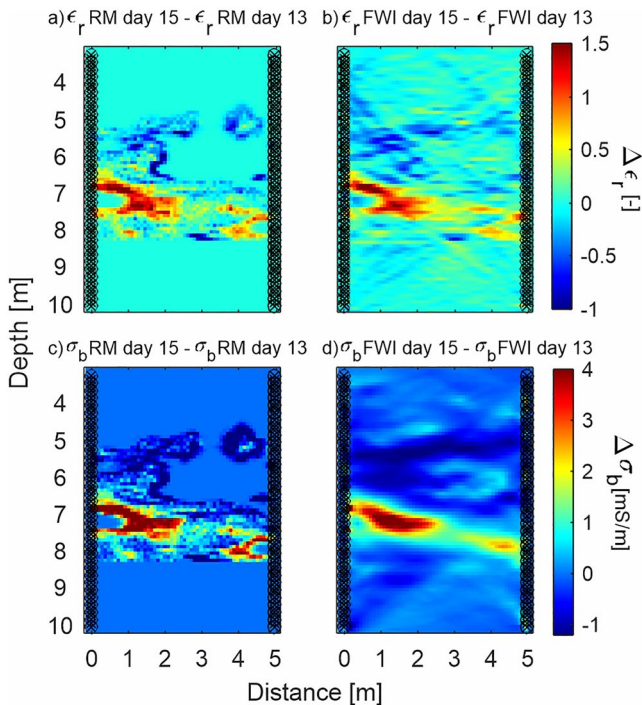


**Figure 15.** Tracer distribution changes between day 15 and day 13 based on permittivity: (a) Real and (b) full-waveform inversion (FWI) recovered models and based on bulk conductivity: (c) Real and (d) FWI recovered models.

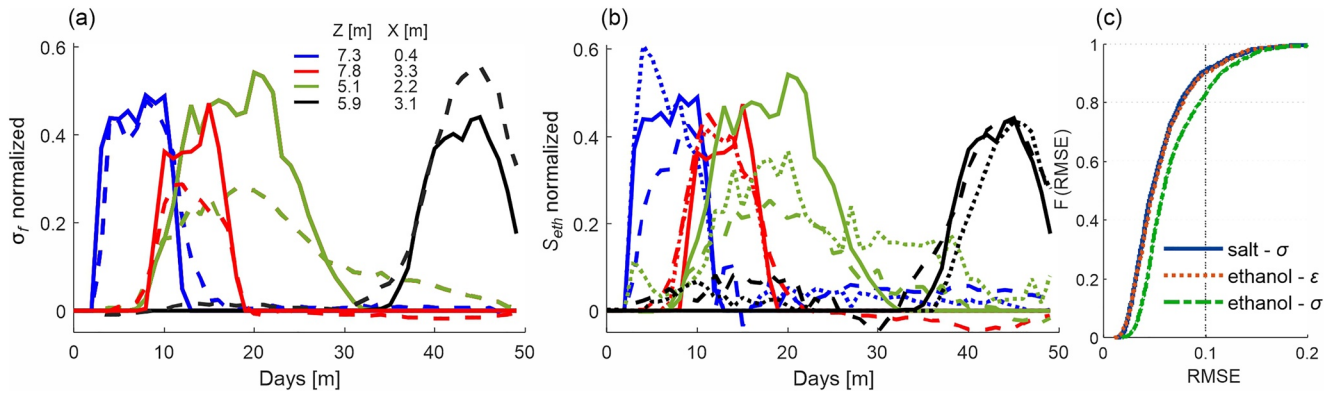


**Figure 16.** Recovered tracer breakthrough curves at single cells from full-waveform inversion (FWI) parameters. Breakthrough curves for days 0–49 drawn at four locations in the crosshole plane (see legend) in the plane for the (a) salt and (b) ethanol tracers. The breakthrough curves are normalized to the maximal true  $\sigma_f$  (salt test) and  $S_{eth}$  (ethanol test) in the entire aquifer volume, respectively. The true tracer, and the tracer recovered from permittivity and conductivity are presented by continuous, dotted and dashed lines, respectively. (c) Cumulative distribution function (CDF) from all-cells of root-mean-squared error of the breakthrough curves, for the recovered tracer that was derived from salt (from  $\sigma_b$ ) and from ethanol (from  $\epsilon_r$  and from  $\sigma_b$ ). 2,444 breakthrough curve locations cells were used for the CDF.

To assess which tracer test and which FWI parameter recovered BTCs the most accurately, we used the RMSE of the BTCs at all cells to calculate the cumulative distribution function (CDF, Figure 16c). Low values of RMSE and a similar CDF are observed for normalized  $\sigma_f$  (salt) derived from  $\sigma_b$  and for normalized  $S_{eth}$  (ethanol) from  $\epsilon_r$ , while for  $S_{eth}$  (ethanol) derived from  $\sigma_b$  RMSE is higher. The larger normalized error of  $\sigma_b$ -derived  $S_{eth}$  (ethanol) than the normalized error of the salt tracer is due to the larger change in  $\sigma_b$  caused by the *Intermediate* salinity tracer than by the ethanol tracer.

## 6. Considerations for Experimental Tracer Test

Overall, we have demonstrated a high potential of the FWI to recover tracer from time-lapse crosshole GPR data. Especially in contrast to the ray-based results, the FWI can reconstruct the medium parameters with high resolution resolving small-scale structures within the decimeter-scale and allows detecting tracers that mainly affect the electrical conductivity. Nevertheless, for the application to experimental data, several issues and challenges should be considered.

### 6.1. 3D Versus 2D GPR Wave Behavior

The crosshole GPR FWI is currently mainly applied in 2D due to computational limitations for 3D approaches. Therefore, diffracted energy from out-of-plane scatters, and specifically in the case of heterogeneous tracer concentration, cannot be considered. Applying a 2D FWI to 3D measured/simulated data, can cause several issues that should be considered in the results evaluation of experimental data. Two main problems arise by inverting 3D data with a 2D inversion. First is the out-of-plane effect on the GPR signals, which is not simulated with a 2D forward model. Second is the errors introduced by the 3D to 2D transformation of measured GPR data for experimental data application (e.g., Klotzsche, Vereecken, & van der Kruk, 2019). Note that for our presented synthetic study both effects are not incorporated.

To investigate out-of-plane effects on the 3D and 2D data, we can apply two approaches. One way is to estimate the zone of influence on the GPR data. The Fresnel zone of the used GPR signals indicates the sampling zone for the cross-borehole signals. The Fresnel zone can be described by a 3D ellipsoid volume (Fresnel volume), which depends on the distance between the antennas, the center frequency of the signals, and permittivity of the medium. Generally, the radius of the first Fresnel zone  $R_{FR}$  is approximated for a monochromatic wavelength  $\lambda$  (Schuster, 1996):

$$R_{FR} = \sqrt{\frac{\lambda \cdot x_0}{2}}, \quad (10)$$

where  $x_0$  is half the crosshole distance ( $L$ ), and  $\lambda$  ( $L$ ) is depending on  $\epsilon_r$  and  $f$ . To evaluate the effect of the Fresnel zone in a tracer experiment due to out-of-plane effects, we compare  $R_{FR}$  with the horizontal correlation length ( $I_h$ ) of  $\ln K$ , which dominates the distribution of the plume in the flow direction. For the aquifer conditions and acquisition setup in this study, the minimum, average and maximum of  $\epsilon_r$  result in  $R_{FR}$  of 0.96, 1.23 and 1.83 m, respectively. Thus, in the main Facies 2 the  $R_{FR}$  for the average  $\epsilon_r$  is smaller than the horizontal correlation length  $I_h = 1.75$  m and, larger than the vertical  $I_v = 0.18$  m. Therefore, for the size of  $R_{FR}$ , there are small spatial variations in out-of-plane direction, but large spatial model variations in the in-plane vertical direction. As a result, out-of-plane effects in these crosshole measurements have a relatively low weight in the overall signal. Using FWI with 2D data and for an  $R_{FR}$  of 1.23 m, features with a size of about 0.2 m could be resolved in the vertical direction (Figure 7), and also at a decimeter scale for a real GPR data (in 3D) in Krauthausen aquifer (e.g., Gueting et al., 2017). This shows that FWI of an extensive and dense data set can get better model resolution than expected from the magnitude of the Fresnel zone.

Additionally, we performed some modeling tests and compared 3D, 2.5D, and 2D GPR data of an exemplary day after a salt tracer injection to investigate the effect of plume heterogeneity on the data itself. A detailed description can be found in Text S4 and Figure S6 of Supporting Information S1. Our tests, which considered a day with a strong out-of-plane  $\sigma$  contrast, indicate that in 3D and 2.5D data only minor differences are shown in the phase and amplitude, mainly where off-plane scatterers are present. Overall, the out-of-plane effects on the GPR data seem to be minor (comparing 2.5D and 3D data), and probably related to the zone of influence on the signal. It is expected that they will not change the inversion results significantly, since the phase and amplitude differences will probably not change gradient directions because the out-of-plane travel paths cannot be explained by the travel paths in-plane that are used by the FWI.

A larger effect and hence influence on the final 2D FWI tomograms is associated with the 3D to 2D transformation filter of the GPR data to allow a 2D FWI (Bleistein, 1986). We performed for our 3D data a 3D-to-2D conversion, resulting in “semi 2D” GPR data (Figures S6b–S6d in Supporting Information S1). Mozaffari et al. (2020) demonstrated that this transformation mainly affects late arrival amplitudes of the measured data in the presence of high contrast layers, which results in a difference of approximately 2% between 2.5D and 2D FWI results for both  $\epsilon_r$  and  $\sigma_b$ . A similar behavior can be seen in our tests. Especially in the zone where the tracer is present, which causes a high contrast (Figure S6a in Supporting Information S1, right), late arrival data is affected and a mismatch between the 2D and “semi 2D” is present. These errors are introduced by the Bleistein filter, because one assumption of the filter is that the highest amplitude of the data is associated with the first arrival times. But in the presence of high contrast zones, which can cause wave interferences, this assumption is not always valid and hence the amplitudes are not accurately correct toward 2D. Note that the Bleistein filter for data outside the tracer region performs well and a good fit between the 2D and “semi 2D” can be observed (Figure S6d in Supporting Information S1, receiver at 5.5 m). As expected the “semi 2D” data in the presence of the high contrast tracer show some errors in the amplitude of the wavelets (Figure S6d in Supporting Information S1, receiver at 6.58, 7.66 m) and hence will affect the electrical conductivity results.

Overall, it seems that the out-of-plane effects on the GPR data are minor and the errors introduced by the 3D to 2D conversion are probably larger. As a result, only 3D GPR FWI and to a lesser extent 2.5D, which consider the 3D medium and plume heterogeneity, can minimize such errors. Although a 2.5D FWI method in the time domain exists (Mozaffari et al., 2020), to analyze a high number of data sets is currently not feasible due to the high computation costs, as just for a single forward run it is 10 times larger than for a 2D forward run.

## 6.2. Time-Lapse Data Acquisition

To improve the quantitative values mainly of the  $\sigma_b$  FWI results and decrease the uncertainties of the results, Oberröhrmann et al. (2013) and Keskinen et al. (2021) indicated that a dense transmitter and receiver spacing during the acquisition should be used. Such acquisitions are time consuming and should not be applied during a tracer experiment, where shorter temporal changes are expected. Therefore, we propose to measure a dense background data set that is able to reconstruct the medium with a good accuracy, which is then used as a starting model for the time-lapse data that is sampled with a larger spacing. To improve the  $\sigma_b$  results in the region of the expected tracer, a denser transmitter sampling could be used for a limited domain. For large contrasts in permittivity due to tracer changes, cycle-skipping between the starting model's background and time-lapse data should

be carefully checked to set the wavelength criteria. In case that criterion is not met, another approach should be adopted, for example, ray-based permittivity inversion from that time-lapse data.

### 6.3. Temporal Tracer Changes During Crosshole GPR Data Collection

In our studies, we assumed quasi-static conditions for each FWI and time-step. For experimental data acquisition this is of course not the case and if the GPR data collection is slower than the dynamic process of tracer transport, this could cause changes in the aquifer for GPR measurements during the survey period. From our experience in crosshole GPR field measurements, for the amount of data considered in this study (7 m depth interval in both boreholes using a transmitter and receiver spacing 0.2 and 0.1 m, respectively), data collection takes about 3 hr. From the transport modeling results (Figure 12, top row) under realistic aquifer conditions the plume's leading front and center is transported at about 3 m/day and 1 m/day, respectively. This results in approximately 0.375 and 0.125 m transport distance in 3 hr. These transport distances are shorter than the Fresnel Zone. Thus, transport changes in the aquifer during GPR measurements occur across distances shorter than the GPR sampling zone, and therefore are not resolved by GPR. Overall, the effect for the Krauthausen test site is expected to be minor under the mentioned conditions, but this should be judged independently for different aquifers having a higher flow velocity. One approach to reduce the error introduced by data-collection time for crosshole GPR was performed using space-time parameterization and regularization of two sequential data sets (Day-Lewis et al., 2002, 2003), and principally could be applied also to the FWI scheme.

## 7. Conclusions

In this study, we tested the reconstruction of tracer plumes with crosshole GPR FWI in a numerical experiment. Realistic dimensions of the plume and the electrical aquifer properties influenced by it were derived from available aquifer and tracer test data sets from previous studies at the Krauthausen test site. We used this information to generate a high-resolution aquifer model and to run transport simulations. We tested the GPR FWI to reconstruct the plume for a saline and desalinated tracers, which changed  $\sigma_b$ , and an ethanol tracer, which changed both  $\epsilon_r$  and  $\sigma_b$ , and found that the resolution obtained with FWI was much higher than ray-based inversion.

We added random instrumental noise to the synthetic data and found that FWI fitted the data successfully, except for when the tracer attenuated the signal too much. Similar aquifer structures and only a minor statistical degrade in comparison to FWI noise-free data was obtained due to instrumental noise. We showed that as long as the data amplitude is higher than the level of the random noise, and not attenuated too much due to the presence of the tracer, the FWI reconstructs the plume successfully.

We tested four different strategies to define the optimal starting model of the time-lapse data. Thereby it was shown that using the FWI of the previous day (strategy III), the FWI images contain more spectral information in comparison to the background starting model, however the tomograms showed a lower model accuracy. One reason for this could be that numerical model errors are accumulated in the recovered FWI models, which are then sequentially further propagated in the following inversion resulting in overfitting causing more numerical artifacts. Therefore, using FWI background (strategy II) is found as a robust and practical FWI starting model strategy for time-lapse data, adequate for all tracer experiments.

FWI Recovery of both permittivity and electrical conductivity distributions resolved structures of about 0.2 m. While the electrical conductivity structures are more smoothed and the anomalies in the model are more dampened, the permittivity model is able to reconstruct more details. Therefore, the reconstruction of the plume from GPR time-lapse data sets and using petrophysical relations which depend both on porosity (from FWI permittivity background) and formation factor (from FWI electrical conductivity background), provided better reconstruction of permittivity changes. The high-resolved reconstructed distribution of the tracer allowed us to calculate breakthrough curves which successfully recovered the true ones, at each cell in the cross-borehole plane.

We showed by estimating the approximated first Fresnel volume (zone which affects the GPR traveling wave) and by performing 3D modeling, that out-of-plane effects which include the heterogeneity of the elongated plume, do not significantly affect the signal. Because the horizontal distribution of the plume is relatively uniform within the Fresnel zone radius, for synthetic 2D data that is generated in a crosshole plane perpendicular to the flow



direction, out-of-plane effects of the heterogeneity of the plume will not dominate the recorded signals. Thus, for the realistic tracer transport heterogeneity, investigating GPR FWI with 2D data is acceptable, and saves computation time in comparison to simulating 3D data for multiple days in a tracer test. In addition, changes in concentrations during acquisition time were small and it was acceptable to neglect these changes. However, in aquifers with a fast transport velocity, this assumption would require further testing.

To summarize, the ability to monitor and locate environmental tracers using two GPR FWI parameters at a high-resolution, shows the potential of time-lapse GPR FWI in practical applications, for example, to locate and monitor pollutants and remediation injection liquids.

## Data Availability Statement

Hydrological and geophysical data sets from Krauthausen test site are open in public domain of the TERENO database (<https://ddp.tereno.net/ddp/geonet.jsp>, “Krauthausen test site,” file identifier ad404c9f-419a-4b14-b6e0-6ee9acd8f80e).

## Acknowledgments

This study is part of the Enigma ITN program (European training Network for in situ imaging of dynamic processes in heterogeneous subsurface environments). This project has received funding from the European Union's Horizon 2020 research and innovation programme under the Marie Skłodowska-Curie Grant Agreement No 722028. The measurements we used to generate the aquifer model were funded by the “TERrestrial ENvironmental Observatories” (TERENO). The computing time was granted by the John von Neumann Institute for Computing and provided on the supercomputer JURECA at Jülich Supercomputing Centre. The authors thank Kamini Singha (editor), Andrew Binley (associate editor), François Lavoué (reviewer) and an anonymous reviewer for their constructive reviews. Open access funding enabled and organized by Projekt DEAL.

## References

- Annan, A. P. (2009). Electromagnetic principles of ground penetrating radar. *Ground Penetrating Radar: Theory and Applications*, 1, 1–37. <https://doi.org/10.1016/b978-0-444-53348-7.00001-6>
- Archie, G. E. (1942). The electrical resistivity log as an aid in determining some reservoir characteristics. *Transactions of the AIME*, 146(1), 54–62. <https://doi.org/10.2118/942054-g>
- Asnaashari, A., Brossier, R., Garambois, S., Audebert, F., Thore, P., & Virieux, J. (2015). Time-lapse seismic imaging using regularized full-waveform inversion with a prior model: Which strategy? *Geophysical Prospecting*, 63(1), 78–98. <https://doi.org/10.1111/1365-2478.12176>
- Axtell, C., Murray, T., Kulassa, B., Clark, R. A., & Gusmeroli, A. (2016). Improved accuracy of cross-borehole radar velocity models for ice property analysis. *Geophysics*, 81(1), WA203–WA212. <https://doi.org/10.1190/geo2015-0131.1>
- Bechtold, M., Vanderborght, J., Ippisch, O., & Vereecken, H. (2011). Efficient random walk particle tracking algorithm for advective-dispersive transport in media with discontinuous dispersion coefficients and water contents. *Water Resources Research*, 47(10). <https://doi.org/10.1029/2010wr010267>
- Binley, A., Hubbard, S. S., Huisman, J. A., Revil, A., Robinson, D. A., Singha, K., & Slater, L. D. (2015). The emergence of hydrogeophysics for improved understanding of subsurface processes over multiple scales. *Water Resources Research*, 51(6), 3837–3866. <https://doi.org/10.1002/2015wr017016>
- Birchak, J. R., Gardner, C. G., Hipp, J. E., & Victor, J. M. (1974). High dielectric constant microwave probes for sensing soil moisture. *Proceedings of the IEEE*, 62(1), 93–98. <https://doi.org/10.1109/proc.1974.9388>
- Bleistein, N. (1986). Two-and-one-half dimensional in-plane wave propagation. *Geophysical Prospecting*, 34(5), 686–703. <https://doi.org/10.1111/j.1365-2478.1986.tb00488.x>
- Carmichael, R. S. (1988). *Practical handbook of physical properties of rocks and minerals*. CRC Press.
- Cheng, A. H., & Bear, J. (2016). *Modeling groundwater flow and contaminant transport*. Springer Publishing Company.
- Dafflon, B., Irving, J., & Barrash, W. (2011). Inversion of multiple intersecting high-resolution crosshole GPR profiles for hydrological characterization at the Boise Hydrogeophysical Research Site. *Journal of Applied Geophysics*, 73(4), 305–314. <https://doi.org/10.1016/j.jappgeo.2011.02.001>
- Daniels, D. J. (2004). *Ground penetrating radar*. The Institution of Electrical Engineers.
- Day-Lewis, F. D., Harris, J. M., & Gorelick, S. M. (2002). Time-lapse inversion of crosswell radar data. *Geophysics*, 67(6), 1740–1752. <https://doi.org/10.1190/1.1527075>
- Day-Lewis, F. D., Lane, J. W., Jr., Harris, J. M., & Gorelick, S. M. (2003). Time-lapse imaging of saline-tracer transport in fractured rock using difference-attenuation radar tomography. *Water Resources Research*, 39(10). <https://doi.org/10.1029/2002wr001722>
- Day-Lewis, F. D., Singha, K., & Binley, A. M. (2005). Applying petrophysical models to radar travel time and electrical resistivity tomograms: Resolution-dependent limitations. *Journal of Geophysical Research*, 110(B8), B08206. <https://doi.org/10.1029/2004jb003569>
- Englert, A. (2003). *Measurement, estimation and modelling of groundwater flow velocity at Krauthausen test site* (Doctoral dissertation). Bibliothek der RWTH Aachen.
- Everett, M. E. (2013). *Near-surface applied geophysics*. Cambridge University Press.
- Friedman, S. P. (2005). Soil properties influencing apparent electrical conductivity: A review. *Computers and Electronics in Agriculture*, 46(1–3), 45–70. <https://doi.org/10.1016/j.compag.2004.11.001>
- Glaser, D. R., Werkema, D. D., Versteeg, R. J., Henderson, R. D., & Rucker, D. F. (2012). Temporal GPR imaging of an ethanol release within a laboratory-scaled sand tank. *Journal of Applied Geophysics*, 86, 133–145. <https://doi.org/10.1016/j.jappgeo.2012.07.016>
- Gomez, D. E., & Alvarez, P. J. (2009). Modeling the natural attenuation of benzene in groundwater impacted by ethanol-blended fuels: Effect of ethanol content on the lifespan and maximum length of benzene plumes. *Water Resources Research*, 45(3). <https://doi.org/10.1029/2008wr007159>
- Gringarten, E., & Deutsch, C. V. (2001). Teacher's aide variogram interpretation and modeling. *Mathematical Geology*, 33(4), 507–534. <https://doi.org/10.1023/a:1011093014141>
- Guetting, N., Caers, J., Comunian, A., Vanderborght, J., & Englert, A. (2018). Reconstruction of three-dimensional aquifer heterogeneity from two-dimensional geophysical data. *Mathematical Geosciences*, 50(1), 53–75. <https://doi.org/10.1007/s11004-017-9694-x>
- Guetting, N., Klotzsche, A., van der Kruk, J., Vanderborght, J., Vereecken, H., & Englert, A. (2015). Imaging and characterization of facies heterogeneity in an alluvial aquifer using GPR full-waveform inversion and cone penetration tests. *Journal of Hydrology*, 524, 680–695. <https://doi.org/10.1016/j.jhydrol.2015.03.030>
- Guetting, N., Klotzsche, A., van der Kruk, J., Vanderborght, J., Vereecken, H., & Englert, A. (2020). Corrigendum to "Imaging and characterization of facies heterogeneity in an alluvial aquifer using GPR full-waveform inversion and cone penetration tests" [J. Hydrol. (2015) 680–695]. *Journal of Hydrology*, 590, 125483. <https://doi.org/10.1016/j.jhydrol.2020.125483>

- Gueting, N., Vienken, T., Klotzsche, A., van der Kruk, J., Vanderborght, J., Caers, J., et al. (2017). High resolution aquifer characterization using crosshole GPR full-waveform tomography: Comparison with direct-push and tracer test data. *Water Resources Research*, 53(1), 49–72. <https://doi.org/10.1002/2016wr019498>
- Hagrey, A. (2000). GPR study of pore water content and salinity in sand. *Geophysical Prospecting*, 48(1), 63–85. <https://doi.org/10.1046/j.1365-2478.2000.00180.x>
- Hermans, T., Wildemeersch, S., Jamin, P., Orban, P., Brouyère, S., Dassargues, A., & Nguyen, F. (2015). Quantitative temperature monitoring of a heat tracing experiment using cross-borehole ERT. *Geothermics*, 53, 14–26. <https://doi.org/10.1016/j.geothermics.2014.03.013>
- Holliger, K., Musil, M., & Maurer, H. R. (2001). Ray-based amplitude tomography for crosshole georadar data: A numerical assessment. *Journal of Applied Geophysics*, 47(3–4), 285–298. [https://doi.org/10.1016/s0926-9851\(01\)00072-6](https://doi.org/10.1016/s0926-9851(01)00072-6)
- Huisman, J. A., Hubbard, S. S., Redman, J. D., & Annan, A. P. (2003). Measuring soil water content with ground penetrating radar: A review. *Vadose Zone Journal*, 2(4), 476–491. <https://doi.org/10.2136/vzj2003.0476>
- Jackson, P. D., Smith, D. T., & Stanford, P. N. (1978). Resistivity-porosity-particle shape relationships for marine sands. *Geophysics*, 43(6), 1250–1268. <https://doi.org/10.1190/1.1440891>
- Johnson, D. L., Koplik, J., & Schwartz, L. M. (1986). New pore-size parameter characterizing transport in porous media. *Physical Review Letters*, 57(20), 2564–2567. <https://doi.org/10.1103/physrevlett.57.2564>
- Kemna, A., Vanderborght, J., Kulesa, B., & Vereecken, H. (2002). Imaging and characterisation of subsurface solute transport using electrical resistivity tomography (ERT) and equivalent transport models. *Journal of Hydrology*, 267(3–4), 125–146. [https://doi.org/10.1016/s0022-1694\(02\)00145-2](https://doi.org/10.1016/s0022-1694(02)00145-2)
- Keskinen, J., Looms, M. C., Klotzsche, A., & Nielsen, L. (2021). Practical data acquisition strategy for time-lapse experiments using crosshole GPR and full-waveform inversion. *Journal of Applied Geophysics*, 191, 104362. <https://doi.org/10.1016/j.jappgeo.2021.104362>
- Klotz, D. (1977). *Berechnung der Filtergeschwindigkeit einer Grundwasserströmung aus Tracerverdünnungsversuchen in einem Filterpegel* (Technical report). GSF. GSF-Bericht R149.
- Klotz, D. (1990). *Berechnete Durchlässigkeiten handelsüblicher Brunnenfilterrohre und Kunststoff-Kiesbelagfilter* (Technical report, Vol. 35). GSF. GSF-Bericht Nr.
- Klotzsche, A., Lärm, L., Vanderborght, J., Cai, G., Morandage, S., Zörner, M., et al. (2019). Monitoring soil water content using time-lapse horizontal borehole GPR data at the field-plot scale. *Vadose Zone Journal*, 18(1), 190044. <https://doi.org/10.2136/vzj2019.05.0044>
- Klotzsche, A., van der Kruk, J., Bradford, J., & Vereecken, H. (2014). Detection of spatially limited high porosity layers using crosshole GPR signal analysis and full-waveform inversion. *Water Resources Research*, 50(8), 6966–6985. <https://doi.org/10.1002/2013WR015177>
- Klotzsche, A., van der Kruk, J., Meles, G. A., Doetsch, J., Maurer, H., & Linde, N. (2010). Full-waveform inversion of cross-hole ground-penetrating radar data to characterize a gravel aquifer close to the Thur River, Switzerland. *Near Surface Geophysics*, 8(6), 635–649. <https://doi.org/10.1109/icgpr.2010.5550238>
- Klotzsche, A., van der Kruk, J., Meles, G. A., & Vereecken, H. (2012). Crosshole GPR full-waveform inversion of waveguides acting as preferential flow paths within aquifer systems. *Geophysics*, 77(4), H57–H62. <https://doi.org/10.1190/geo2011-0458.1>
- Klotzsche, A., Vereecken, H., & van der Kruk, J. (2019). Review of crosshole ground-penetrating radar full-waveform inversion of experimental data: Recent developments, challenges, and pitfalls. *Geophysics*, 84(6), H13–H28. <https://doi.org/10.1190/geo2018-0597.1>
- Lavoué, F., Brossier, R., Métivier, L., Garambois, S., & Virieux, J. (2015). Frequency-domain modelling and inversion of electromagnetic data for 2D permittivity and conductivity imaging: An application to the Institut Fresnel experimental dataset. *Near Surface Geophysics*, 13(3), 227–241. <https://doi.org/10.3997/1873-0604.2015004>
- Li, W., Englert, A., Cirpka, O. A., Vanderborght, J., & Vereecken, H. (2007). Two-dimensional characterization of hydraulic heterogeneity by multiple pumping tests. *Water Resources Research*, 43(4). <https://doi.org/10.1029/2006wr005333>
- Lide, D. R. (Ed.). (2004). *CRC handbook of chemistry and physics* (Vol. 85). CRC Press.
- Looms, M. C., Jensen, K. H., Binley, A., & Nielsen, L. (2008). Monitoring unsaturated flow and transport using cross-borehole geophysical methods. *Vadose Zone Journal*, 7(1), 227–237. <https://doi.org/10.2136/vzj2006.0129>
- Maliva, R. G. (2016). *Aquifer characterization techniques*. Springer.
- Malmberg, C. G., & Maryott, A. A. (1956). Dielectric constant of water from 0° to 1000°C. *Journal of Research of the National Bureau of Standards*, 56, 1. <https://doi.org/10.6028/jres.056.001>
- McDowell, C. J., Buscheck, T., & Powers, S. E. (2003). Behavior of gasoline pools following a denatured ethanol spill. *Ground Water*, 41(6), 746–757. <https://doi.org/10.1111/j.1745-6584.2003.tb02416.x>
- Meles, G. A., Van der Kruk, J., Greenhalgh, S. A., Ernst, J. R., Maurer, H., & Green, A. G. (2010). A new vector waveform inversion algorithm for simultaneous updating of conductivity and permittivity parameters from combination crosshole/borehole-to-surface GPR data. *IEEE Transactions on Geoscience and Remote Sensing*, 48(9), 3391–3407. <https://doi.org/10.1109/tgrs.2010.2046670>
- Mozaffari, A., Klotzsche, A., Warren, C., He, G., Giannopoulos, A., Vereecken, H., & van der Kruk, J. (2020). 2.5D crosshole GPR full-waveform inversion with synthetic and measured data. *Geophysics*, 85(4), 1–51. <https://doi.org/10.1190/geo2019-0600.1>
- Mualem, Y., & Friedman, S. P. (1991). Theoretical prediction of electrical conductivity in saturated and unsaturated soil. *Water Resources Research*, 27(10), 2771–2777. <https://doi.org/10.1029/91wr01095>
- Müller, K., Vanderborght, J., Englert, A., Kemna, A., Huisman, J. A., Rings, J., & Vereecken, H. (2010). Imaging and characterization of solute transport during two tracer tests in a shallow aquifer using electrical resistivity tomography and multilevel groundwater samplers. *Water Resources Research*, 46(3). <https://doi.org/10.1029/2008wr007595>
- Oberröhrmann, M., Klotzsche, A., Vereecken, H., & van der Kruk, J. (2013). Optimization of acquisition setup for cross-hole GPR full-waveform inversion using checkerboard analysis. *Near Surface Geophysics*, 11(2), 197–209. <https://doi.org/10.3997/1873-0604.2012045>
- Personna, Y. R., Slater, L., Ntarlagiannis, D., Werkema, D., & Szabo, Z. (2013). Electrical signatures of ethanol–liquid mixtures: Implications for monitoring biofuels migration in the subsurface. *Journal of Contaminant Hydrology*, 144(1), 99–107. <https://doi.org/10.1016/j.jconhyd.2012.10.011>
- Petong, P., Pottel, R., & Kaatz, U. (2000). Water–ethanol mixtures at different compositions and temperatures. A dielectric relaxation study. *The Journal of Physical Chemistry A*, 104(32), 7420–7428. <https://doi.org/10.1021/jp001393r>
- Remy, N., Boucher, A., & Wu, J. (2009). *Applied geostatistics with SGeMS: A user's guide*. Cambridge University Press.
- Rhoades, J. D. (1981). Predicting bulk soil electrical conductivity versus saturation paste extract electrical conductivity calibrations from soil properties. *Soil Science Society of America Journal*, 45(1), 42–44.
- Schuster, G. T. (1996). Resolution limits for crosswell migration and traveltimes tomography. *Geophysical Journal International*, 127(2), 427–440. <https://doi.org/10.1111/j.1365-246x.1996.tb04731.x>
- Singha, K., & Gorelick, S. M. (2005). Saline tracer visualized with three-dimensional electrical resistivity tomography: Field-scale spatial moment analysis. *Water Resources Research*, 41(5). <https://doi.org/10.1029/2004wr003460>

- Spalding, R. F., Toso, M. A., Exner, M. E., Hattan, G., Higgins, T. M., Sekely, A. C., & Jensen, S. D. (2011). Long-term groundwater monitoring results at large, sudden denatured ethanol releases. *Groundwater Monitoring & Remediation*, 31(3), 69–81. <https://doi.org/10.1111/j.1745-6592.2011.01336.x>
- Sreenivas, K., Venkatarantan, L., & Rao, P. N. (1995). Dielectric properties of salt-affected soils. *International Journal of Remote Sensing*, 16(4), 641–649. <https://doi.org/10.1080/01431169508954431>
- Tillmann, A., Englert, A., Nyári, Z., Fejes, I., Vanderborght, J., & Vereecken, H. (2008). Characterization of subsoil heterogeneity, estimation of grain size distribution and hydraulic conductivity at the Krauthausen test site using cone penetration test. *Journal of Contaminant Hydrology*, 95(1–2), 57–75. <https://doi.org/10.1016/j.jconhyd.2007.07.013>
- van der Kruk, J., Gueting, N., Klotzsche, A., He, G., Rudolph, S., von Hebel, C., et al. (2015). Quantitative multi-layer electromagnetic induction inversion and full-waveform inversion of crosshole ground penetrating radar data. *Journal of Earth Science*, 26(6), 844–850. <https://doi.org/10.1007/s12583-015-0610-3>
- Van der Schaaf, V. A., & van Hateren, J. V. (1996). Modelling the power spectra of natural images: Statistics and information. *Vision Research*, 36(17), 2759–2770. [https://doi.org/10.1016/0042-6989\(96\)00002-8](https://doi.org/10.1016/0042-6989(96)00002-8)
- Vereecken, H., Döring, U., Hardelauf, H., Jaekel, U., Hashagen, U., Neuendorf, O., et al. (2000). Analysis of solute transport in a heterogeneous aquifer: The Krauthausen field experiment. *Journal of Contaminant Hydrology*, 45(3–4), 329–358. [https://doi.org/10.1016/S0169-7722\(00\)00107-8](https://doi.org/10.1016/S0169-7722(00)00107-8)
- Vereecken, H., Lindenmayr, G., Neuendorf, O., Döring, U., & Seidemann, R. (1994). *TRACE: A mathematical model for reactive transport in 3D variable saturated porous media* (ICG-4 internal report 501494). Forschungszentrum Jülich GmbH.
- Wyman, J. (1931). The dielectric constant of mixtures of ethyl alcohol and water from  $-5$  to  $40^\circ$ . *Journal of the American Chemical Society*, 53(9), 3292–3301. <https://doi.org/10.1021/ja01360a012>
- Zhang, Z., & Huang, L. (2013). Double-difference elastic-waveform inversion with prior information for time-lapse monitoring. *Geophysics*, 78(6), R259–R273. <https://doi.org/10.1190/geo2012-0527.1>
- Zhou, Z., Klotzsche, A., Hermans, T., Nguyen, F., Schmäck, J., Haruzi, P., et al. (2020). 3D aquifer characterization of the Hermalle-sous-Argenteau test site using crosshole GPR amplitude analysis and full-waveform inversion. *Geophysics*, 85(6), H133–H148. <https://doi.org/10.1190/geo2020-0067.1>
- Zhou, Z., Klotzsche, A., & Vereecken, H. (2021). Improving crosshole ground-penetrating radar full-waveform inversion results by using progressively expanded bandwidths of the data. *Near Surface Geophysics*, 19(4), 465–487. <https://doi.org/10.1002/nsg.12154>

## References From the Supporting Information

- Belina, F., Irving, J., Ernst, J., & Holliger, K. (2012). Analysis of an iterative deconvolution approach for estimating the source wavelet during waveform inversion of crosshole georadar data. *Journal of Applied Geophysics*, 78, 20–30. <https://doi.org/10.1016/j.jappgeo.2011.05.003>
- Berenger, J. P. (1994). A perfectly matched layer for the absorption of electromagnetic waves. *Journal of Computational Physics*, 114(2), 185–200. <https://doi.org/10.1006/jcph.1994.1159>
- Bialas, Z., & Kleczkowski, A. (1970). *Über den praktischen Gebrauch von einigen empirischen Formeln zur Berechnung des Durchlässigkeitskoeffizienten K*. Archivum Hydrotechniki.
- Giannopoulos, A. (2011). Unsplit implementation of higher order PMLs. *IEEE Transactions on Antennas and Propagation*, 60(3), 1479–1485. <https://doi.org/10.1109/tap.2011.2180344>
- Kelter, M., Huisman, J. A., Zimmermann, E., & Vereecken, H. (2018). Field evaluation of broadband spectral electrical imaging for soil and aquifer characterization. *Journal of Applied Geophysics*, 159, 484–496. <https://doi.org/10.1016/j.jappgeo.2018.09.029>
- Peterson, J. E., Jr. (2001). Pre-inversion corrections and analysis of radar tomographic data. *Journal of Environmental & Engineering Geophysics*, 6(1), 1–18. <https://doi.org/10.4133/jee6.1.1>
- Warren, C., Giannopoulos, A., & Giannakis, I. (2016). gprMax: Open source software to simulate electromagnetic wave propagation for Ground Penetrating Radar. *Computer Physics Communications*, 209, 163–170. <https://doi.org/10.1016/j.cpc.2016.08.020>